AIAA AVIATION Forum
June 25-29, 2018, Atlanta, Georgia
2018 Fluid Dynamics Conference

10.2514/6.2018-3704

Amplification and Structure of Streamwise-Velocity Fluctuations in Four Shock-Wave/Turbulent Boundary-Layer Interactions

M. A. Mustafa* N. J. Parziale†
Stevens Institute of Technology, Hoboken, NJ 07030, USA
M. S. Smith‡ E. C. Marineau§¶
AEDC White Oak, Silver Spring, MD 20903, USA

In this work, we study the effect of compression-corner angle on streamwise turbulent kinetic energy (sTKE) and structure in Mach 2.8 flow. Krypton Tagging Velocimetry (KTV) is used to investigate the incoming turbulent boundary layer and flow over 8°, 16°, 24° and 32° compression corners. The experiments were performed in a 99% N_2 and 1% Kr gas mixture in the AEDC Mach 3 Calibration Tunnel (M3CT). A figure of merit is defined as the wall-normal integrated mean of the sTKE ($\overline{\text{sTKE}}$) which is designed to identify turbulence amplification by accounting for the root-mean-squared (RMS) velocity fluctuations and shear-layer width for the different geometries. We observe that the $\overline{\text{sTKE}}$ increases as an exponential with compression-corner angle near the root when normalized by the boundary-layer value. Additionally, snapshot proper orthogonal decomposition (POD) is applied to the KTV results to investigate the structure of the flow. From the POD results, we extract the dominant flow structures and compare each case by presenting mean-velocity maps that correspond to the largest positive and negative POD mode coefficients. Finally, the POD spectrum reveals an inertial range common to the boundary-layer and each compression-corner flow that is present after the first ≈ 10 dominant POD modes.

Nomenclature

x	= Streamwise coordinate, (-)
y	= Wall-normal coordinate, (-)
M	= Mach Number, (-)
P	= Pressure, (Pa)
ρ	= Density, (kgm^{-3})
γ	= Ratio of specific heats, (-)
T	= Temperature, (K)
Re	= Reynold's number, (-)
Pr	= Prandlt number, (-)
u	= Streamwise velocity component, (m s^{-1})
v	= Normal velocity component, (m s^{-1})
u'	= Fluctuating streamwise velocity component, (m s^{-1})
v'	= Fluctuating normal velocity component, (m s^{-1})
U	= Mean streamwise velocity component, (m s^{-1})
δ	= Boundary layer thickness, (m)
u_τ	= Friction velocity, (m s^{-1})

*Graduate Student, Mechanical Engineering, Castle Point on Hudson, Hoboken, New Jersey, 07030.
†Assistant Professor, Mechanical Engineering, Castle Point on Hudson, Hoboken, New Jersey, 07030, Senior AIAA Member.
‡Senior Research Engineer, National Aerospace Solutions, Silver Spring, MD 20903, Senior AIAA Member
§Chief Technologist, AEDC White Oak, Silver Spring, MD 20903, Senior AIAA Member.
¶Currently Program Officer, Hypersonics, Office of Naval Research Code 351, Arlington, VA 22203, Senior AIAA Member.

θ = Wedge angle, (degrees)
θ_s = Shear layer angle, (degrees)
β = Wave angle, (degrees)
Θ = Momentum thickness, (-)
$R_{u'u'}$ = Longitudinal correlation coefficient, (-)
x_{01} = Shear layer origin, (-)
ζ = Similarity variable, (-)
ϕ = POD modes, (-)
a_{ij} = POD mode coefficient, (m s^{-1})
C_{ij} = Correlation matrix, (m^2 s^{-2})
λ = Eigenvalue, (m^2 s^{-2})
E_{tot} = Total energy from eigenvalues, (m^2 s^{-2})
e_{ij} = Eigenvector, (-)
L_1 = Structure length, (-)
L_2 = Structure thickness, (-)
θ_{st} = Structure angle, (degrees)

Subscript
RMS = Root mean squared
∞ = Free stream
w = Wall
Θ = Based on momentum thickness
BL = Based on boundary layer data

I. Introduction

The interaction of shock waves and boundary layers is a fundamental problem in high-speed flow physics motivated by practical applications. Dolling[1] states "[shock-wave boundary-layer interactions] are ubiquitous in high-speed flight, occurring in an almost limitless number of external and internal flow problems relevant to aircraft, missiles, rockets, and projectiles. Maximum mean and fluctuating pressure levels and thermal loads that a structure is exposed to are generally found in regions of shock/boundary-layer and shock/shear-layer interaction and can effect vehicle and component geometry, structural integrity, material selection, fatigue life, the design of thermal protection systems, weight, and cost." Consequently, to better design high-speed vehicles it is necessary to understand the fundamentals of this complex interaction. This ubiquity has led to a plethora of computational[2–6] and experimental[7–12] investigations into this interaction. Reviews[13–15] highlight the current state of the research.

The breadth of interactions is vast, as discussed in the introductory chapters of Babinski and Harvey.[16] In this work, we focus our study on the effect of compression-corner angle on streamwise turbulent kinetic energy (sTKE) and structure in Mach 2.8 flow. For example, this canonical flow may be observed in practice as the deflection of a control surface on a vehicle in high-speed flight or in the flow path of a high-speed, air-breathing engine. Trends of velocity-fluctuation amplitude and turbulence structure with compression-corner angle imply a change in the shear stress, heat-transfer rate, and mixing properties of the flow, all of which have simulation and design implications.

An important feature of SWBLI is the modification of turbulence stresses across the flow field. Experimental investigations have determined that there are significant turbulent amplifications across shocks. Smits et al.[10] studied the shock-wave/turbulent boundary-layer interaction over three compression corners and reported amplification factors of 4-15 for the mass-flux fluctuation intensity, and even larger factors for the shear stresses. Humble et al.[11] used particle image velocimetry (PIV) to study the flow over a flat plate with an impinging shock and found amplification factors on the same order of magnitude as Smits et al.[10] Computational efforts have also provided similar insight. In the direct numerical simulation (DNS) of Wu et al.,[5] amplifications factors of 6-24 for the Reynolds stresses were calculated for a Mach 2.9 flow over a 24° compression ramp. Using large eddy simulation (LES), Porter et al.[17] report amplification factors of 2.3-7.6 for the Reynolds stresses for a Mach 2.25 flow over a 24° compression ramp.

Another important feature of turbulent flow is the existence of structures of various time and length scales.[18] In regions of SWBLI, it is expected that the behavior of these structures is even more complicated because of the various interactions. Being able to quantify these scales and deepening our understanding of the physical properties and relative importance of these structures will further improve our ability to model turbulent flows. An analytical tool that accomplishes this is proper orthogonal decomposition (POD). It was first introduced to the fluid dynamics community by Lumley[19,20] as a means to extract coherent structures from flow fields. A nice review of POD analysis in the broader context of modal analysis can be found in Taira et al.[21] The fundamental idea of POD is to decompose the velocity field into a series of modes weighted based on the amount of kinetic energy they contain, each of which can be interpreted as a coherent structure. This technique has been used to study combustion engines,[22–24] turbulent flow over a fence,[25] open cavity flow,[26] axisymmetric jet flow and mixing layers[27] and the turbulent flow over a cylinder,[28] to name a few. There are not many applications of POD to SWBLIs in the literature. One example is that of Piponniau et al.[29] where a POD analysis was performed on PIV results from an induced-shock-wave/turbulent boundary-layer interaction. The authors aimed to investigate "the unsteady breathing of the recirculating bubble at low frequency and the Kelvin-Helmholtz instabilities developing at moderate frequency."

We begin this paper by describing the experimental facility, the Mach 3 Calibration Tunnel (the M3CT), and the measurement technique, Krypton Tagging Velocimetry (KTV). Then, we establish that the incoming flow is nominally a canonical, turbulent boundary layer over a flat plate by reporting KTV measurements of mean- and fluctuating-velocity profiles and comparing them to those found in the literature. We then report results of mean- and fluctuating-velocity profiles of flows over 8°, 16°, 24° and 32° compression corners which yields a case-wise comparison of streawise turbulent kinetic energy (sTKE). Finally, we apply POD to the KTV results and discuss the eigen-spectra and make case-wise comparisons of the most energetic POD modes.

II. Facility and Experimental Setup

The experiments were performed in the Arnold Engineering Development Complex (AEDC) Mach 3 Calibration Tunnel (M3CT) in Silver Spring, MD (Fig. 1). The tunnel is comprised of a large vacuum tank attached to a converging diverging nozzle. An orifice plate was added upstream of the nozzle as in Zahradka et al.[30] and Mustafa et al.[31] to control the freestream pressure. A flexible isolation bag was added upstream of the orifice to contain the 99% N_2/1% Kr gas mixture. The flexibility ensured that the bag stayed at the constant ambient pressure of the laboratory. A valve is cycled downstream of the nozzle to run the tunnel. The run condition calculations can be found in Zahradka et al.[30] and Mustafa et al.[31] Conditions are listed in Table 1.

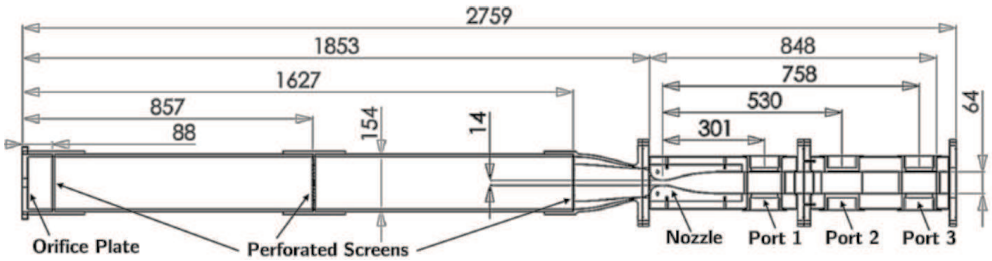

Figure 1: Sketch of AEDC Mach 3 Calibration Tunnel (M3CT). Dimensions in millimeters. The measurements are made at "Port 2."

Table 1: M_∞, P_∞, T_∞, ρ_∞, $\mathrm{Re}_\infty^{unit}$, Re_Θ, and U_∞ are the Mach number, pressure, temperature, density, unit Reynolds number, momentum-thickness Reynolds number, and velocity for the AEDC M3CT tunnel with the 19.1 mm orifice plate.

M_∞ (-)	P_∞ (Pa)	T_∞ (K)	ρ_∞ (kg/m^3)	$\mathrm{Re}_\infty^{unit}$ (1/m)	Re_Θ (-)	U_∞ (m/s)
2.77	1010	118	0.030	2.30e6	1750	612

To ensure that the M3CT started properly and to visualize the shock-wave/turbulent boundary-layer interaction structures, a Z-type schlieren[32] setup was used to visualize the flow field over the compression corners. The schlieren setup consisted of a sparklamp light source and an Integrated Design Tools N3 camera recording at 100 frames-per-second with a 50 ns exposure time. The knife-edge was set as a horizontal cutoff. Fig. 2 shows the mean of 100 exposures of the schlieren visualization for each wedge with the mean shock position marked, as determined by local curve fitting to the image intensity.

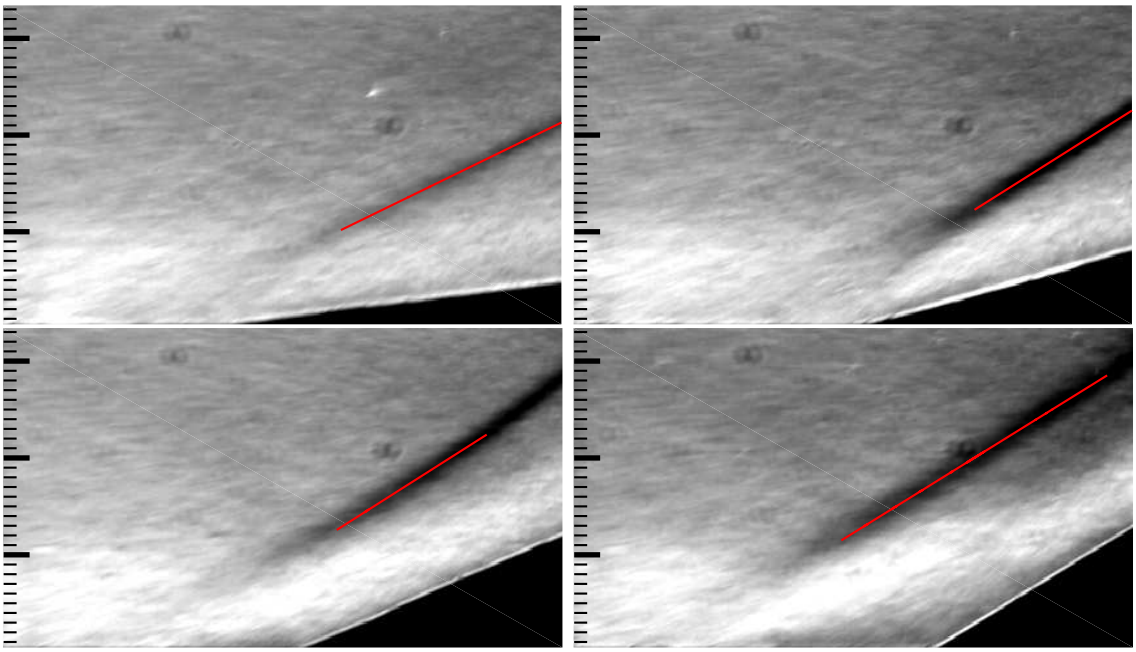

Figure 2: Clockwise from top-left are the mean schlieren images for the 8, 16, 32 and 24 degree corners, respectively. Flow is left to right. Major tick marks are at 10 mm. Mean shock position shown in red.

To compare the flow field investigated in the present work with that in the literature, the mean initial shock angles (β) are plotted in Fig. 3 against the wedge angle θ. The graph shows that for the 8° wedge, β is equal to the calculated value from inviscid theory. Beginning with the 16° wedge, β approaches a constant value of $\approx 32°$. This trend of β approaching a constant value is is in agreement with the work by Spaid and Frishett[33] (which was at Mach 2.9), which is also plotted in Fig. 3. The value of β for the 8° and 16° wedge is in agreement with previous work by Smits and Muck.[10] The initial shock angle for the 24° wedge is in agreement with DNS work by Wu and Martin[5] and experimental work by Settles et al.[8] and Mustafa et al.[31]

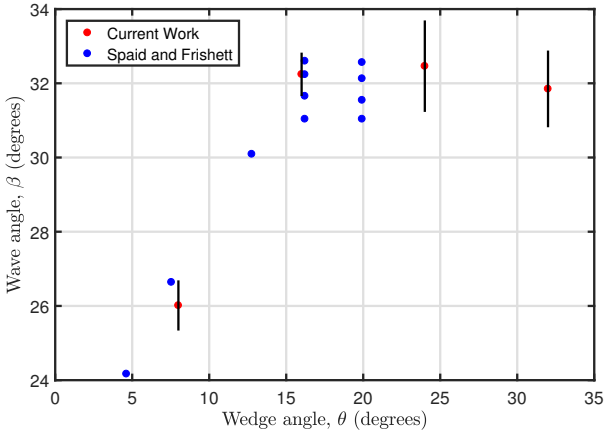

Figure 3: Initial (β) shock angles from schlieren images shown in red. Results from Spaid and Frishett[33] shown in blue. Vertical black bars denote uncertainty.

III. Krypton Tagging Velocimetry (KTV)

Tagging velocimetry is a laser velocimetry technique which is typically performed in gases by tracking the fluorescence of a native, seeded, or synthesized gas. Its advantage over particle-based techniques in high-speed facilities is that it is not limited by timing issues associated with tracer injection[34] or reduced particle response at Knudsen and Reynolds numbers[35] characteristic of high-speed wind tunnels. Methods of tagging velocimetry include the VENOM,[36–40] APART,[41–43] RELIEF,[44–48] FLEET,[49,50] STARFLEET,[51] PLEET,[52] argon,[53] iodine,[54,55] sodium,[56] acetone,[57–59] NH[60] and the hydroxyl group techniques,[61–64] among others.[65–70]

For this work, Krypton Tagging Velocimetry (KTV) was used as the velocimetry technique. The use of a metastable noble gas as a tagging velocimetry tracer was first suggested by Mills et al.[71] and Balla and Everheart.[72] KTV was first demonstrated by Parziale et al.[73,74] to measure the velocity along the center-line of an underexpanded jet of N_2/Kr mixtures. Following that work, Zahradka et al.[30,75] used KTV to make measurements of the mean and fluctuating turbulent boundary-layer profiles in a Mach 2.8 flow. Mustafa et al.[31] used KTV to measure seven simultaneous profiles of streamwise velocity and fluctuations in the incoming boundary layer and immediately upstream of a 24-degree compression corner in a $M_\infty = 2.8$, $\mathrm{Re}_\Theta = 1750$, 99% N_2/1% Kr shock-wave/turbulent boundary-layer interaction. Recently, KTV was implemented in the Stevens Institute of Technology Shock Tube by Mustafa et al.[76] to measure the freestream velocity behind a Mach 3 shock. In addition, KTV has been demonstrated to work in the freestream of the large-scale AEDC Hypervelocity Tunnel 9 at Mach 10 and Mach 14.[77] Preliminary two-dimensional KTV measurements in a Mach 2.8 flow over a 24-degree compression corner were reported in Mustafa et al.[78]

Following the excitation scheme used by Mustafa et al.,[31] KTV is performed in the following steps according to the energy level diagram shown in Fig. 4.

1. Seed a base flow with krypton globally.
2. Photosynthesize metastable krypton atoms with a pulsed tunable laser to form the tagged tracer: two-photon excitation of $4p^6(^1S_0) \rightarrow 5p[3/2]_2$ (214.7 nm) and rapid decay to resonance state $5p[3/2]_2 \rightarrow 5s[3/2]_1^o$ (819.0 nm, transition B) and metastable state $5p[3/2]_2 \rightarrow 5s[3/2]_2^o$ (760.2 nm, transition A). We estimate that the creation of the metastable atoms which comprise the "write line" takes approximately 50 ns.[79] The position of the write line is marked by the fluorescence from the $5p[3/2]_2 \rightarrow 5s[3/2]_1^o$ transitions (819.0 nm, transition B), and is recorded with a camera positioned normal to the flow.
3. Record the displacement of the tagged metastable krypton by imaging the laser induced fluorescence (LIF) that is produced with an additional pulsed tunable laser: excite $5p[3/2]_1$ level by $5s[3/2]_2^o \rightarrow 5p[3/2]_1$ transition with laser sheet (769.5 nm, transition C) and read spontaneous emission of $5p[3/2]_1 \rightarrow 5s[3/2]_1^o$ (829.8 nm, transition D) transitions with a camera positioned normal to the flow.

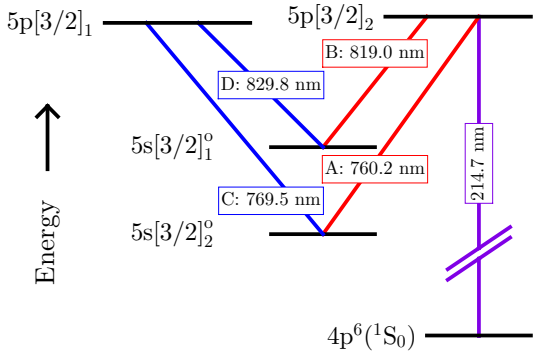

Figure 4: Energy diagram for excitation scheme. Racah nl[K]$_J$ notation, A, B, C and D represent the transitions between the states.

The experiments were run using two tunable lasers to provide the 214.7 nm (write) and 769.5 nm (read) laser beams required for KTV. The write laser consisted of a frequency doubled Quanta Ray Pro-350 Nd:YAG laser and a frequency tripled Sirah PrecisionScan Dye Laser. The Nd:YAG laser pumped the dye laser with 1000 mJ/pulse at a wavelength of 532 nm. The dye in the laser was DCM with a dimethyl sulfoxide (DMSO) solvent, and the laser was tuned to output a 644.1 nm beam. Frequency tripling of the dye-laser output was performed using Sirah tripling optics (THU 205).

The write-laser beam setup can result in approximately 10-13 mJ/pulse; however, approximately 7 mJ was used for this experiment by reducing the Nd:YAG pump-laser power. The wavelength was 214.7 nm, with a linewidth of approximately 0.045 cm^{-1}, a pulsewidth of approximately 7 ns, and a repetition rate of 10 Hz. The write beam was focused into several narrow waists in the test section with a $f = 100$ mm fused-silica microlens array (SUSS MicroOptics Nr. 18-00127) to form the lines in the streamwise direction and a $f = 100$ mm fused-silica cylindrical lens to focus the lines in the spanwise direction. Neglecting losses from the mirrors, lenses, and windows, we estimate that the energy per write line was approximately 350 µJ/pulse.

The read laser consisted of a frequency doubled Quanta Ray Pro-350 Nd:YAG laser and a Sirah PrecisionScan Dye Laser. The Nd:YAG laser pumped the dye laser with 200 mJ/pulse at a wavelength of 532 nm. The dye in the laser was Styryl 8 with a DMSO solvent, and the laser was tuned to output a 769.5 nm beam.

The read-laser beam setup resulted in approximately 5 mJ/pulse, with a wavelength of 769.5 nm, a linewidth of approximately 0.025 cm^{-1}, a pulsewidth of approximately 7 ns, and a repetition rate of 10 Hz. The read-laser beam was directed into the test section using 2 inch broadband dielectric mirrors (Thorlabs BB2-E02), and expanded to a beam of ≈ 40 mm diameter with a $f = -400$ mm BK7 lens. This "read beam" re-excited the metastable Kr tracer atoms so that their displacement could be measured.

The laser and camera timing were controlled by a pulse-delay generator (SRS DG645). The intensified camera used for all experiments was a 16-bit Princeton Instruments PIMAX-4 1024x1024 with an 18-mm grade 1, Gen III extended red filmless intensifier w/ P46 phosphor (PM4-1024i-HR-FG-18-P46-CM). The lens used is a Nikon NIKKOR 24-85mm f/2.8-4D in "macro" mode and positioned approximately 200 mm from the write/read location. Two high-precision 800 nm longpass filters (Thorlabs FELH0800, transmission of 3.5e-4% at the read-laser wavelength of 769.5 nm) were placed in series between the lens and the intensifier to minimize the noise resulting from the read-laser pulse reflection and scatter from solid surfaces. The gain was set to 100% with 1x6 (streamwise x wall-normal) pixel binning and only recording the read images to ensure a 10 Hz frame rate. A set of write images were recorded with the tunnel on prior to each set of experiments. The camera gate was opened for 20 ns immediately following the read-laser pulse to capture the spontaneous emission of $5p[3/2]_1 \rightarrow 5s[3/2]_1^o$ (829.8 nm) transitions.

IV. Boundary-Layer Results

In this section, we present a baseline boundary-layer profile of streamwise velocity and fluctuations. For the boundary-layer results, the write/read delay was set to 500 ns. The KTV setup formed ten lines with appropriate SNR. A sample read exposure is presented as Fig. 5 (left). To process the KTV exposures, the line centers were found in the following way:
1) Crop the image to an appropriate field of view.
2) Apply a two-dimensional Wiener adaptive-noise removal filter.
3) Convert the images to double precision numbers and normalize the intensity to fall in the range of 0-1.
4) Apply the Gaussian peak finding algorithm from O'Haver[80] to find the line centers for the top row using the read lines in the top row of each image as a first guess. This is simple to do in the approximately steady freestream.
5) Proceeding from the top-down, apply the Gaussian peak finding algorithm from O'Haver[80] to find the line centers for each row using the line center location immediately above as the guess.

The dimensional velocity is presented in Fig. 5 (right) as measured by KTV from the present work and PIV from Brooks et al.[81–84] in the same facility. Error bars for the KTV measurements are calculated in the

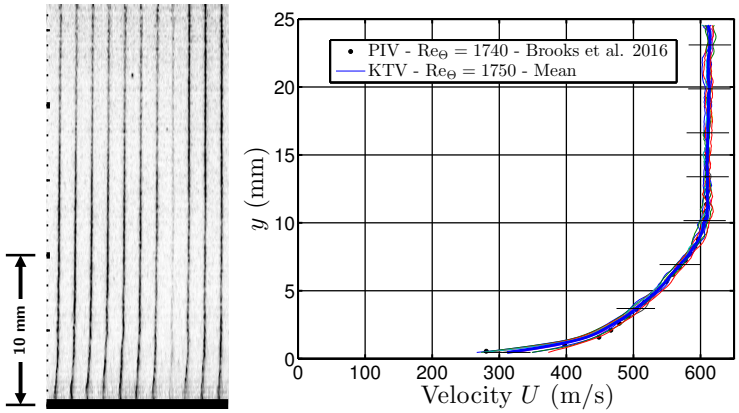

Figure 5: *Left:* Example of KTV boundary-layer fluorescence exposure. Major tick marks are 10 mm. Flow is left to right. Inverted intensity scale. Wall marked as black. *Right:* Dimensional velocity of the Mach 2.8 turbulent boundary layer. Error bars in black.

same fashion as Zahradka et al.[30] as

$$\delta U_{\mathrm{KTV}} = \left[\left(\delta\Delta x \frac{\partial U}{\partial \Delta x} \right)^2 + \left(\delta\Delta t \frac{\partial U}{\partial \Delta t} \right)^2 + \left(v'_{RMS} \frac{dU}{dy} \Delta t \right)^2 \right]^{\frac{1}{2}}. \tag{1}$$

The uncertainty in the measured displacement distance, Δx, of the metastable tracer is estimated as the 95% confidence bound on the write and read locations from the Gaussian fits. The uncertainty Δt is estimated to be the camera gate width, 20 ns, causing fluorescence blurring as considered in Bathel et al.[85] The third term in Eq. 1 is uncertainty in streamwise velocity due to wall-normal fluctuations in the xy-plane. This formulation is taken from Hill and Klewicki[86] and Bathel et al.[85] The wall-normal fluctuations, v'_{RMS}, are conservatively estimated to be 5% of the edge velocity, which is supported by DNS[87] and PIV experiments.[83]

The error in the KTV measurement is approximately 5% in the freestream, the boundary-layer wake region, and the boundary layer logarithmic region. The error in KTV measurement increases to approximately 10% nearest to the wall. The increase nearest to the wall is mostly due to the third term in Eq. 1. There is an appreciable increase in the wall-normal fluctuations and increase in velocity gradient.

The velocity data for the boundary layer can be compared to the law of the wall in the logarithmic region, $U^+ = \frac{1}{\kappa}\ln(y^+) + C$, by using the Van Driest transformation, with $y^+ = \rho_w u_\tau y/\mu_w$ and $U^+ = U/u_\tau$. Following Bradshaw[88] and Huang and Coleman,[89] the Van Driest transformed velocity is written as

$$U^+_{VD} = \frac{1}{R}\left[\sin^{-1}\left(\frac{R(U^+ + H)}{\sqrt{1 + R^2 H^2}} \right) - \sin^{-1}\left(\frac{RH}{\sqrt{1 + R^2 H^2}} \right) \right], \tag{2}$$

where $R = M_\tau \sqrt{(\gamma - 1)\,\mathrm{Pr}_t\,/2}$, $H = B_q/((\gamma - 1)M_\tau^2)$, $M_\tau = u_\tau/c_w$, and $B_q = q_w/(\rho_w c_p u_\tau T_w)$. We assume the turbulent Prandtl number is $\mathrm{Pr}_t = 0.87$, and, assuming the Reynolds analogy holds, the heat-flux number is $B_q = c_f \rho_e U_e (T_w - T_r)/(2\,\mathrm{Pr}_e\,\rho_w u_\tau T_w)$.[90]

The transformed KTV- and PIV-derived velocity profiles are presented in Fig. 6 (left). Also, in Fig. 6 (left), we plot the viscous sublayer as $U^+_{VD} = y^+$ as well as applying Eq. 2 to the logarithmic law as

$$U^+_{VD} = \frac{1}{\kappa}\ln(y^+) + C \tag{3}$$

with $\kappa = 0.41$ and $C = 5.2$. The transformed velocity follows the law of the wall in the logarithmic region with good agreement.

In Fig. 6 (right), we present the streamwise velocity fluctuation results that are non-dimensionalized by the Morkovin[91] scaling and compare those to the literature.[83,87,92,93] In this work, we were able to resolve far closer to the wall than in the previous effort by Zahradka et al.[30] The agreement between the fluctuation data from the literature and KTV is good to down to $y/\delta \approx 0.050$.

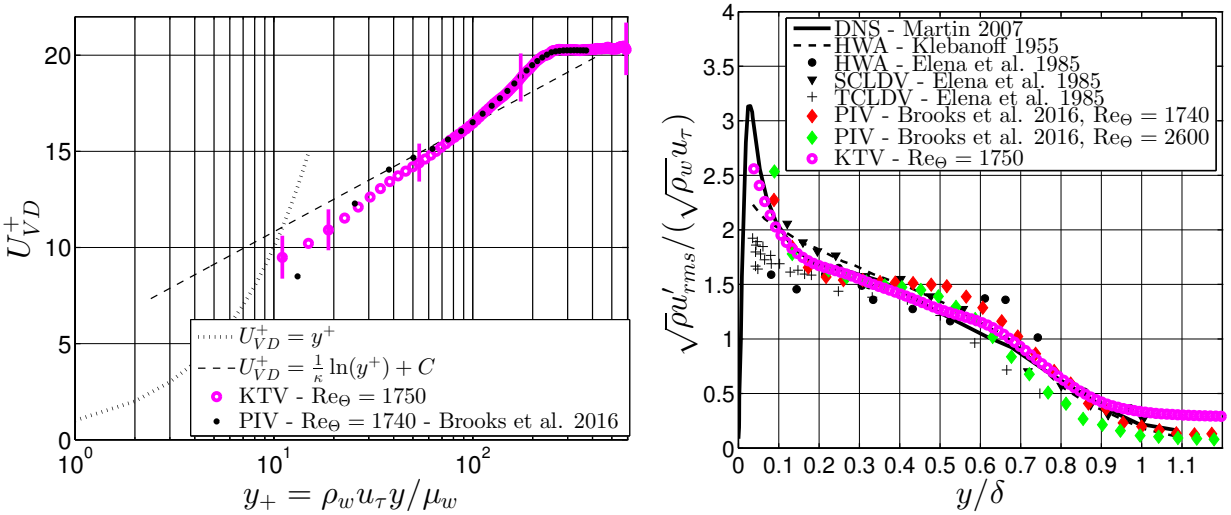

Figure 6: *Left:* Van Driest scaling of the mean velocity. *Right:* Morkovin scaling of streamwise fluctuations.

With the ability to write multiple lines, the longitudinal correlation coefficient can be calculated as

$$f(\mathbf{x}, r) = \frac{\overline{u'(\mathbf{x})u'(\mathbf{x}+r)}}{\overline{u'^2}} = \frac{R_{u'u'}}{\overline{u'^2}} \tag{4}$$

by using the spacing between each write line, r. The longitudinal correlation of the streamwise velocity data are presented as Fig. 7 (left) for $y/\delta \approx 0.2$. As a means of first comparison, $f_{u'u'}$ from the present KTV boundary-layer data is compared to $f_{(\rho u)'(\rho u)'}$ from Duan et al.[94] It should be noted that the work from Duan et al.[94] is at different conditions, $M_\infty = 2.97$, $\mathrm{Re}_\Theta = 3030$.

Moreover, because the flow field should have forwards and backward symmetry, the number of points used for the longitudinal correlation can be increased from 10 to 19 by performing the correlation in Eq. 4 from left-to-right and also right-to-left and concatenating the datasets. This correlation is performed for the field recorded in Fig. 5 for $y/\delta \approx 0.2$ and presented as Fig. 7 (right). Thin horizontal lines in Fig. 7 (right) mark the boundary-layer edge at $y/\delta = 1$ and also the approximate location of the wake-region boundary at $y/\delta \approx 0.41$. Contours of $f_{(\rho u)'(\rho u)'}$ as computed by DNS data from[94] are plotted in black, and contours of $f_{u'u'}$ as measured from KTV data are plotted in red. The KTV data have more scatter, as expected, but the orientation of the contours is quite similar indicating that the average angle of turbulent structures is also similar.

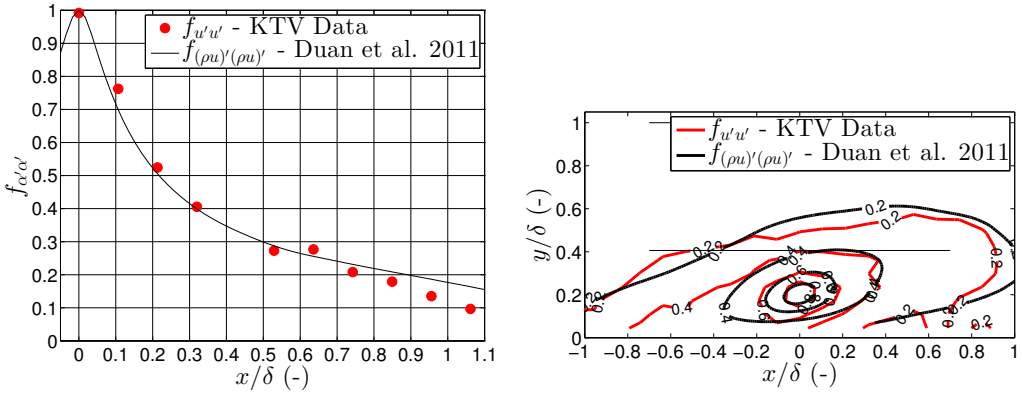

Figure 7: *Left:* Longitudinal correlation for $y/\delta \approx 0.2$. As a means of first comparison, $f_{u'u'}$ from the present KTV boundary-layer data is compared to $f_{(\rho u)'(\rho u)'}$ from Duan et al.[94] *Right:* Contours of correlation. Thin horizontal lines mark the boundary-layer edge and approximate wake-region boundary. KTV data in red, DNS data in black.

In this section, KTV data was compared to that in the literature for a supersonic turbulent boundary layer. From this, we conclude that the nature of the incoming flow can be considered a nominal supersonic turbulent boundary layer enabling the study of shock-wave/turbulent boundary-layer interaction.

V. Shock-Wave/Turbulent Boundary-Layer Interaction Results

In this section, we present the results from experiments designed to investigate turbulent, supersonic corner flows at four different angles: 8, 16, 24, and 32 degrees. This is done by fixing a wedge of the appropriate geometry in Port 2 of the M3CT (see Fig. 1). The root of the corner flow ($x/\delta = 0$) is placed near the center of the boundary-layer measurement location presented in section IV.

Fig. 8 shows sample KTV read exposures for each case. This is the visualization of the $5p[3/2]_1 \rightarrow 5s[3/2]_1^o$ (829.8 nm) transitions. Mach 2.8 flow is left to right and the walls in each corner flow are marked in black. These data are reduced by following the same procedure as in section IV for tracing the profiles in the write and read images.

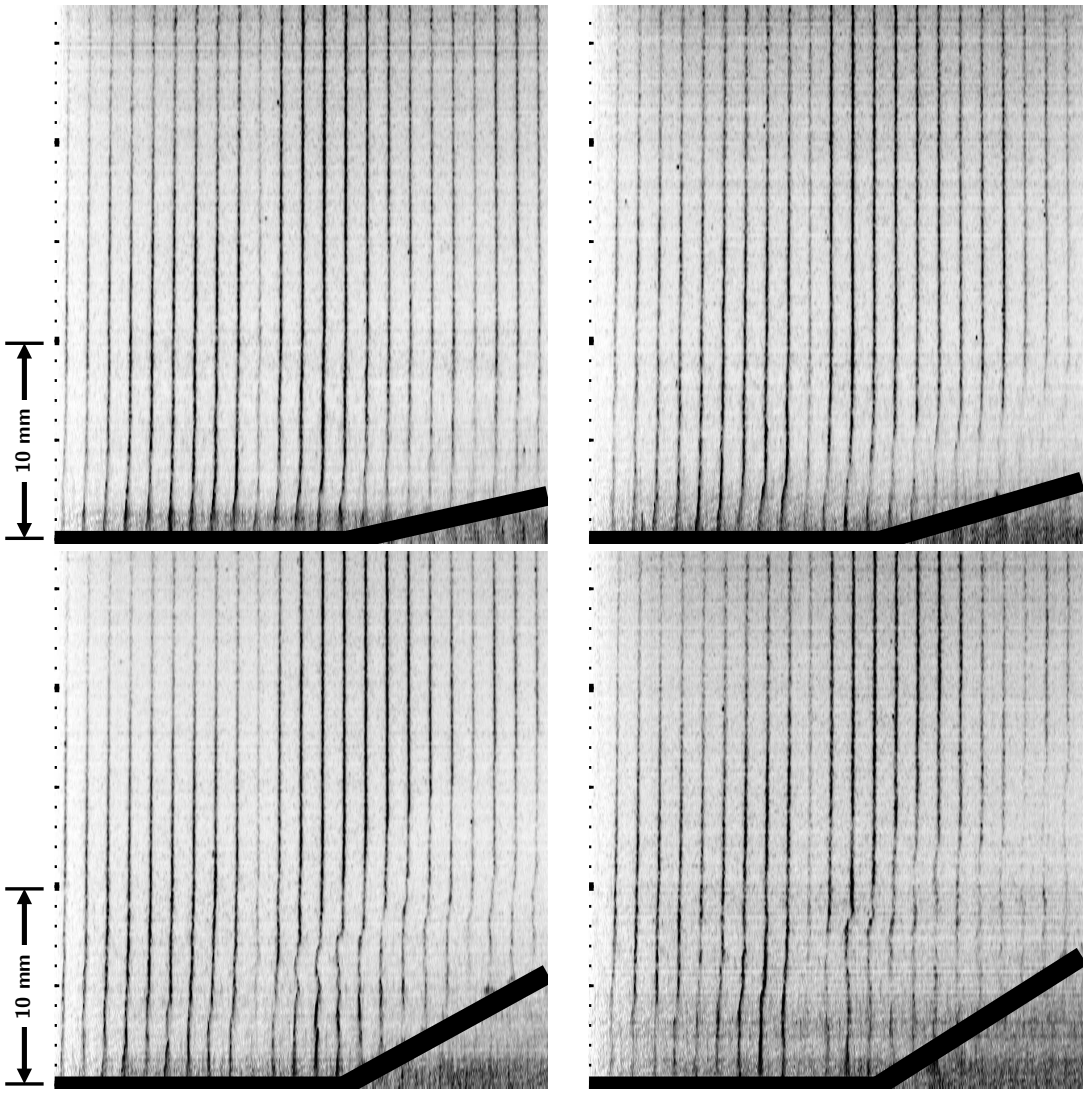

Figure 8: Clockwise from top-left are sample instantaneous shock-wave/turbulent boundary-layer interaction fluorescence exposures for the 8, 16, 32 and 24 degree corners, respectively. These are ostensibly boundary-layer profiles traces with a 500 ns prescribed delay between the write and read step. Major tick marks are 10 mm. Flow is left to right. Inverted intensity scale. Wall marked as black.

Examples of non-dimensional instantaneous velocity profiles ($u/(12U_\infty)$) are presented in Fig. 9. For each corner angle, we show the write location marked as a thin, vertical black line and two example, instantaneous velocity profiles in blue and red. This is intended to visualize relative unsteadiness of each corner flow. Results are not presented within $y/\delta < 0.1$ because the signal to noise ratio was too low to provide data with high confidence. In addition, there is a missing velocity profile every 10 mm because there is a gap between the microlens arrays that yields insufficient focusing and thus low SNR.

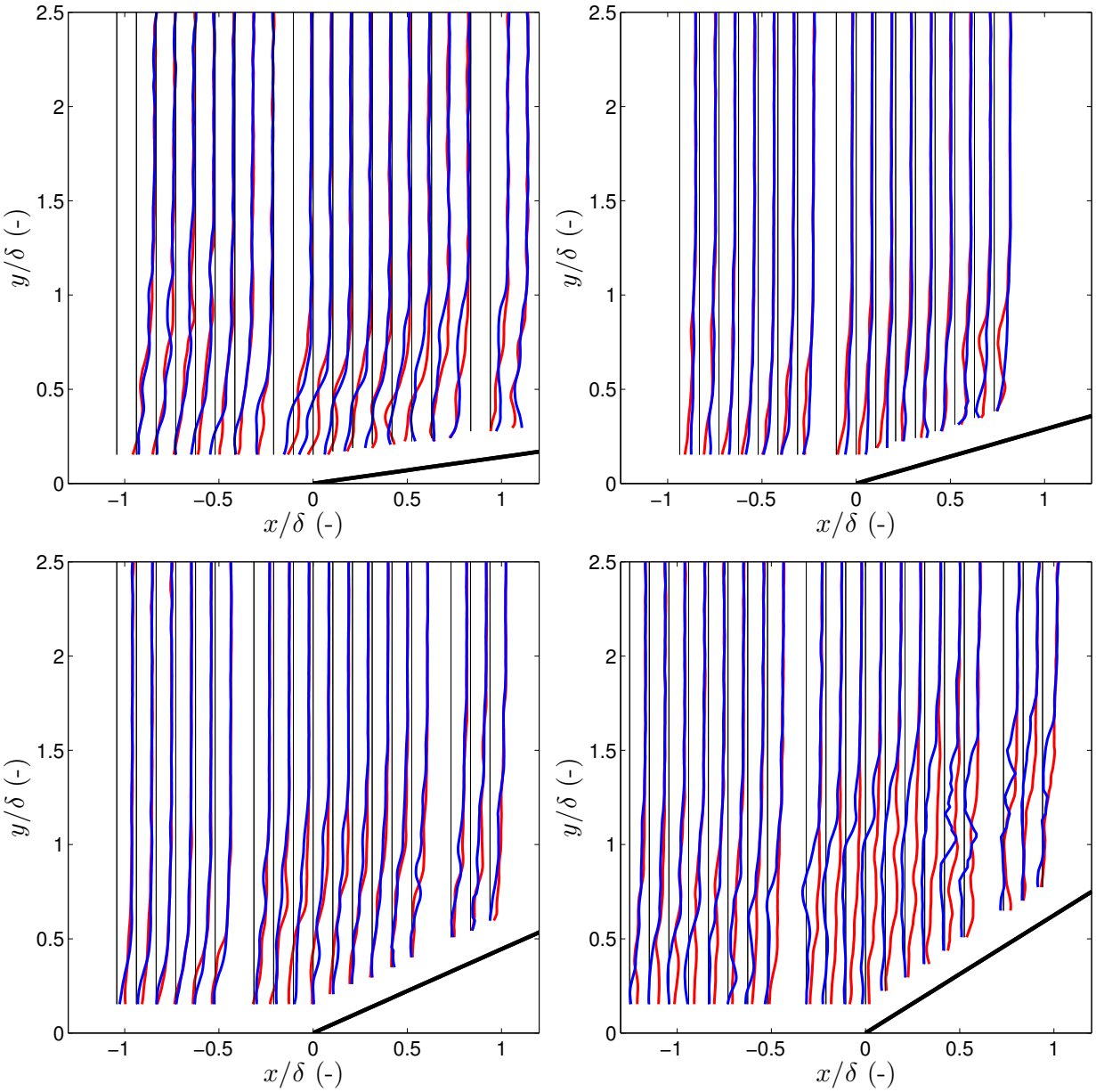

Figure 9: Clockwise from top-left are two sample non-dimensional ($u/(12U_\infty)$), instantaneous shock-wave/turbulent boundary-layer interaction velocity profiles represented in blue and red for the 8, 16, 32 and 24 degree corners, respectively. Thin vertical black line represents the write location. Flow is left to right.

In Fig. 10, we present non-dimensional mean velocity profiles ($u/(12U_\infty)$). For each corner angle, we show the write location marked as a thin, vertical black line and the mean velocity profile as a thicker black line. In the 8 and 16 degree cases, there are no clearly apparent points of inflection in mean profiles. In the 24 degree case, near to the root ($-0.5 \lesssim x/\delta \lesssim 0.5$), and to a much greater extent in the 32 degree case (the

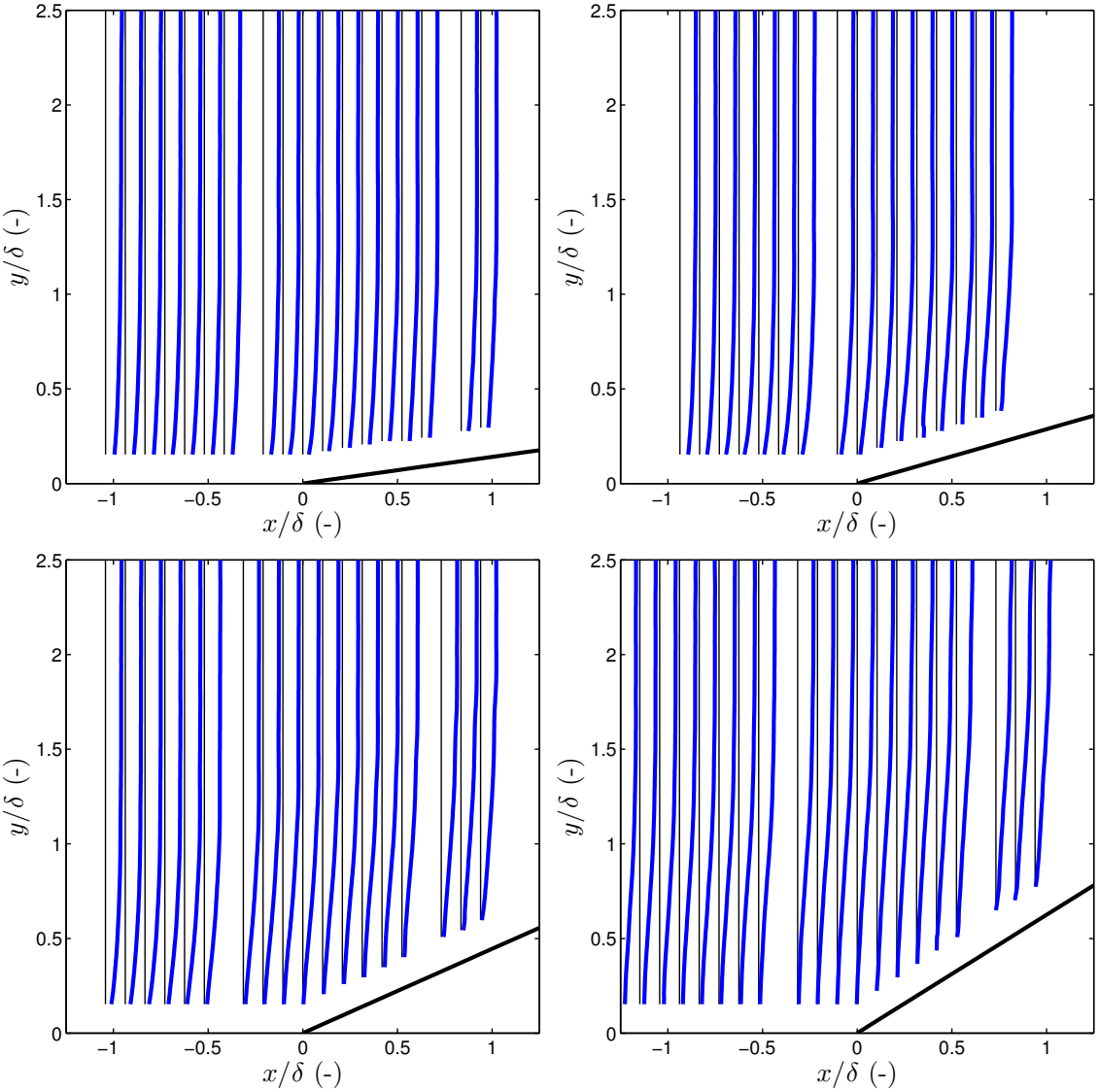

Figure 10: Clockwise from top-left are the non-dimensional $(u/(12U_\infty))$, mean shock-wave/turbulent boundary-layer interaction velocity profiles for the 8, 16, 32 and 24 degree corners, respectively. Thin vertical black line represents the write location. Flow is left to right. Error bars are not plotted because they are not visible at the present scale. We estimate the uncertainty as 5% in the freestream and 15% near the wall.

field of view), there appear to be clear points of inflection in the mean boundary-layer profiles.

Contours of the streamwise component of turbulent kinetic energy (sTKE), $(u'_{RMS})^2/(2U_\infty^2)$, are presented in Fig. 11. For each case, very close to the wall on the ramp, there is a notable increase in fluctuations. This is most likely an artifact of the residual noise from the KTV read step. Despite this, in the 16, 24 and 32 degree cases, a shear layer can clearly be identified as a maxima in fluctuations along a ray inclined at an angle similar to that of the corner angle. No such shear layer was observed in the 8 degree case.

To characterize the shear layers, two parameters were determined: θ_s, which is the angle of the shear-layer coordinate system (x',y') relative to the lab coordinate system (x,y), and x_{01}, which is the origin of the (x',y') coordinate system. The parameters were found by fitting an equation of the form $y = \tan\theta_s(x - x_{01})$ to the spatial locations of the maximum sTKE at each streamwise location. The results for the corners are overlaid on the sTKE contours in Fig. 11 and the values for θ_s and x_{01} are given in Table 2. In performing this analysis it is assumed that the sTKE $(u'^2/(2U_\infty^2))$ is a good surrogate for the total TKE $((u'^2 + v'^2 + w'^2)/(2U_\infty^2))$.

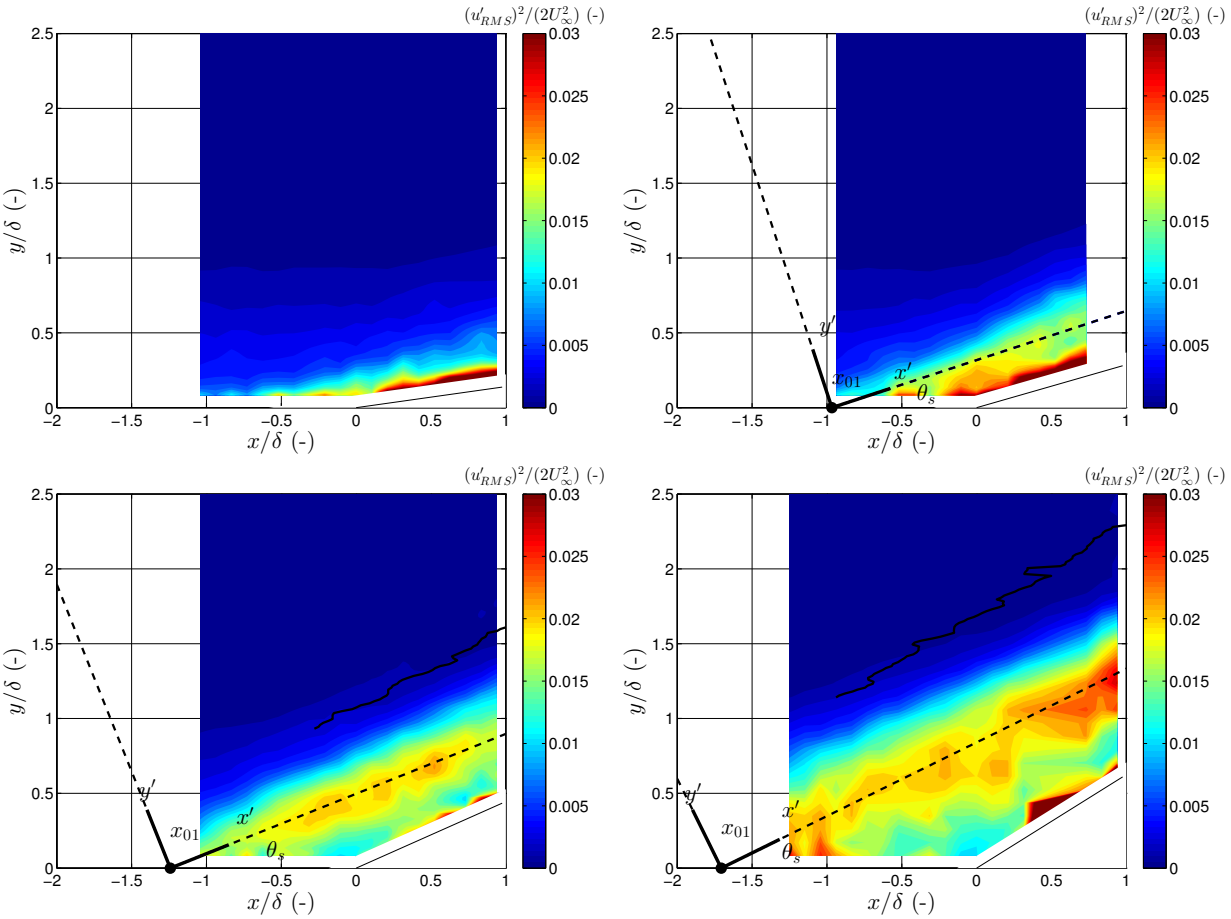

Figure 11: Clockwise from top-left are countours of the non-dimensional streamwise turbulent kinetic energy (sTKE) $(u'_{RMS})^2/(2U_\infty^2)$) for the 8, 16, 32 and 24 degree corners, respectively. The shear layer coordinate system fitted to the maximum sTKE is overlayed. Flow is left to right. Mean shock position shown in black.

Table 2: Shear layer origin, x_{01}, and angle θ_s. Uncertainties estimated as the 95% confidence intervals in the linear fits.

Wedge Angle (Degrees)	x_{01} (-)	θ_s (Degrees)
16	-0.97 ($\pm$ 0.30)	18.2 ($\pm$ 3.9)
24	-1.24 ($\pm$ 0.14)	21.8 ($\pm$ 1.9)
32	-1.71 ($\pm$ 0.27)	26.2 ($\pm$ 3.6)

In Helm et al.,[95] the researchers show that the shear layer over a 24-degree corner may be collapsed in a self-similar fashion. They apply a coordinate transformation to the two-dimensional velocity calculations in the lab frame to determine the velocity in the shear-layer coordinate system. Unfortunately, in this work a rotation may not be applied as the KTV measurements were one dimensional. Despite this, we use the velocity in the lab frame as a surrogate for the velocity in the shear-layer coordinate system and attempt to identify self-similarity to first approximation. In Fig. 12, we attempt to collapse the U/U_2 and u'^2_{RMS}/U_2^2 profiles to a single curve, where U is the mean velocity and U_2 is the velocity downstream of the shock as calculated by the inviscid flow relations for the measured shock angle. The similarity variable used is $\zeta = y'/(x' - x'_{02})$, where x_{02} is the imaginary origin of the shear layer, which is computed by iterating until the profiles collapse. It should be noted that unlike in Helm et al.,[95] u'_{RMS} is the x component of the fluctuating velocity in the (x,y) coordinate system, not the x' component of the fluctuating velocity in the (x',y') coordinate system. Compared to Helm et al.,[95] Fig. 12 shows more scatter and the collapse is

not qualitatively as good. However, despite this and the limitations in the analysis, self-similar behavior is apparent to first approximation.

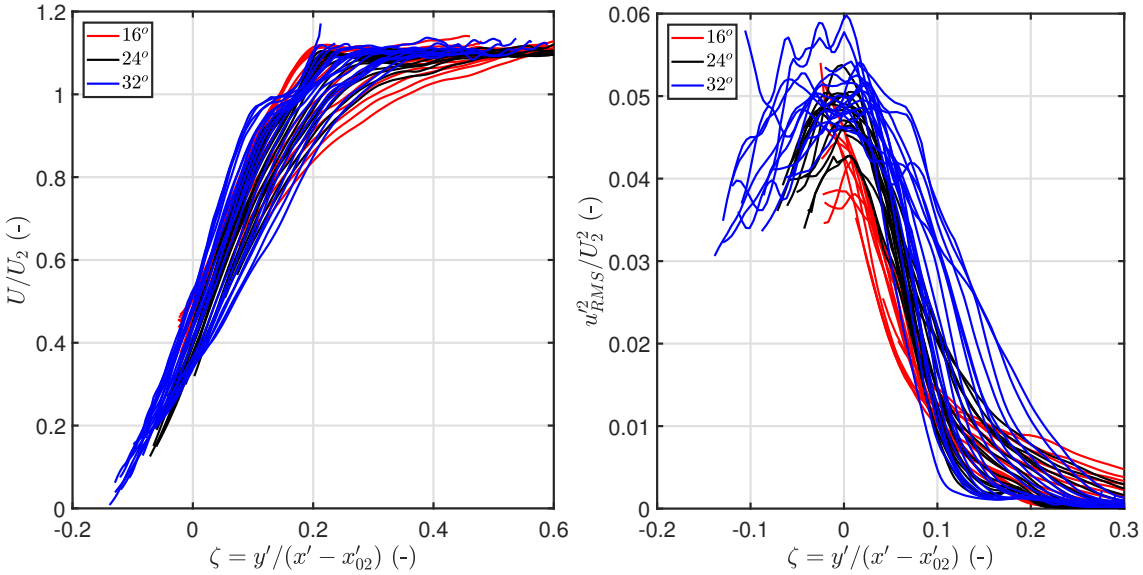

Figure 12: *Left:* U/U_2 profiles plotted against the similarity variable ζ for the 16, 24 and 32 degree corners. *Right:* u'^2_{RMS}/U_2^2 profiles plotted against the similarity variable ζ for the 16, 24 and 32 degree corners. U_2 is the downstream velocity as calculated from oblique shock relations for Mach 2.8 flow and the shock angle as measured form the schlieren images.

VI. Wall-Normal Integrated Mean of Streamwise Turbulent Kinetic Energy

In this section, we present an analysis of the sTKE ($u'^2_{RMS}/2$) in profile form (as opposed to the contours presented earlier) to visualize features in the flow and identify trends in sTKE with compression-corner angle. Profiles of $u'^2_{RMS}/(2U_\infty^2)$ (normalized sTKE) are shown in Fig. 13. The shear layer and the shock wave clearly appear in the 24 and 32 degree cases. These features manifest themselves as two distinct peaks in the sTKE profiles. The 16 degree corner shows a peak at some downstream locations that denotes the shear layer, but the shock is not readily identified. For the 8 degree corner, distinct peaks are not observed.

We define a figure of merit as the wall-normal integrated mean sTKE at a particular streamwise location as

$$\overline{\text{sTKE}} = \frac{1}{2\delta}\int_0^{2\delta} \frac{u'^2_{RMS}}{2U_\infty^2} dy. \tag{5}$$

This figure of merit is designed to identify turbulence amplification by accounting for the RMS velocity fluctuations and shear-layer width for the different geometries. In Fig. 14 (left), we present the $\overline{\text{sTKE}}$ for each streamwise location. It is observed that $\overline{\text{sTKE}}$ increases with increasing x/δ. In Fig. 14 (right), $\overline{\text{sTKE}}$ is plotted against the corner angle at locations downstream of and at the corner. We normalize by the $\overline{\text{sTKE}}$ in the boundary layer (Fig. 6 (right)) to find the effect of compression-corner angle on wall-normal integrated streamwise turbulence amplification. The trend of $\overline{\text{sTKE}}$ with compression-corner angle is found to be an exponential. The parameters for this scaling are given in Table 3 for the two locations. Sensibly, the coefficients of the exponentials in Table 3 are close to unity which implies no amplification at zero compression-corner angle.

Table 3: Sclaing relations for $\overline{\text{sTKE}}$.

x/δ (-)	Fit
0	$\overline{\text{sTKE}}/\overline{\text{sTKE}}_{BL} = 0.90\exp(7.76\text{e-}2\ \theta)$
0.75	$\overline{\text{sTKE}}/\overline{\text{sTKE}}_{BL} = 0.86\exp(8.38\text{e-}2\ \theta)$

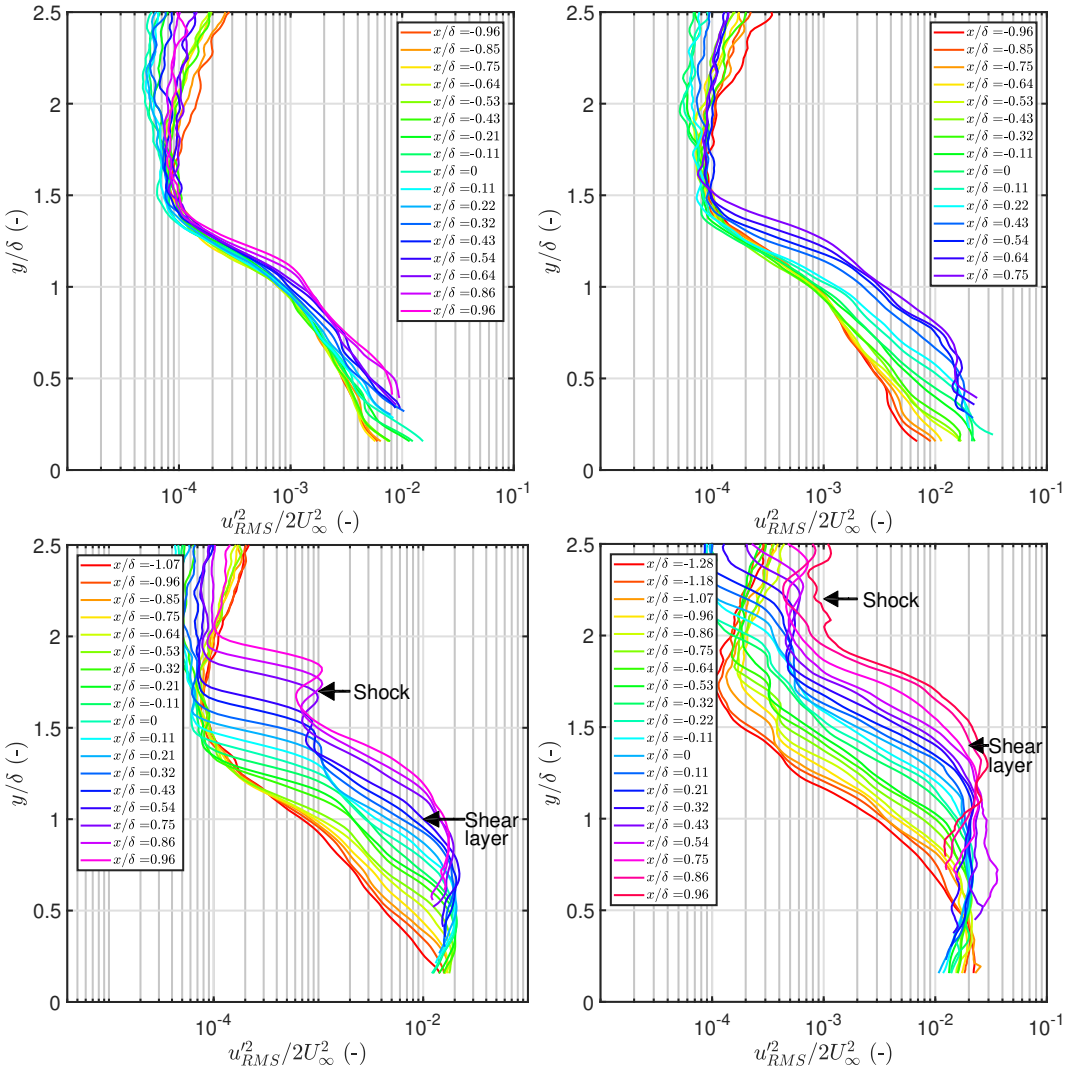

Figure 13: Clockwise from top-left are the $u'^2_{RMS}/(2U_\infty)^2$ profiles at different streamwise locations for the 8, 16, 32 and 24 degree corners, respectively.

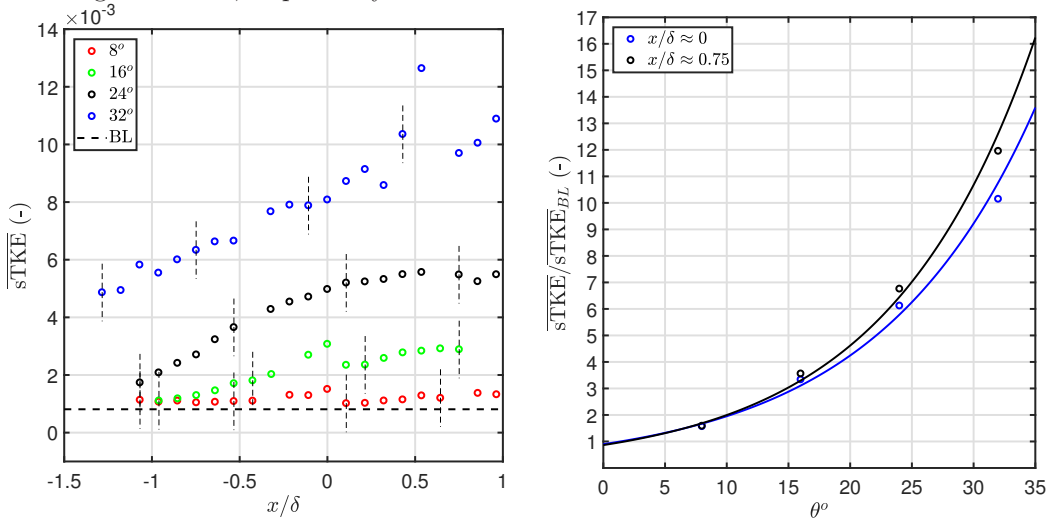

Figure 14: *Left:* Variation of $\overline{\text{sTKE}}$ along streamwise direction for 8, 16, 24 and 32 degree corners. Error bars shown as vertical dashed lines. *Right:* Scaling of $\overline{\text{sTKE}}$ with wedge angle for locations at and downstream of the root, where the values at $x/\delta \approx 0$ are the averages of the points adjacent to and at the root.

VII. Proper Orthogonal Decomposition

The proper orthogonal decomposition (POD) technique can be used to extract spatial and temporal structures from a turbulent flow field.[19–21] This approach decomposes the original vector or scalar field into a weighted, linear sum of basis functions, or modes. In the present work, the instantaneous streamwise velocity fields are recorded at 10 Hz so they are nominally uncorrelated in time; thus, the snapshot method of Sirovitch[96] was chosen to analyze the data. Following the terminology in Sirovitch[96] and Stohr et al.,[97] the velocity fields are decomposed into a mean and fluctuating component as

$$u_i(x,y) = \overline{u}(x,y) + u_i'(x,y), \tag{6}$$

where there are p points in the streamwise direction and q points in the wall-normal direction ($M = p \times q$ total grid points) with N number of snapshots ($i = 1....N$). The fluctuating streamwise velocity field, $u_i'(x,y)$, is reshaped into a matrix, U', with elements $U_i'(X_n)$ where the $n = 1....M$ points for each snapshot form a row for $i = 1....N$ rows, so U' is of dimensions $N \times M$ and can be written as

$$U' = \begin{bmatrix} u_1'(x_1,y_1) & u_1'(x_2,y_1) & .. & u_1'(x_p,y_1) & u_1'(x_1,y_2) & .. & u_1'(x_p,y_q) \\ u_2'(x_1,y_1) & u_2'(x_2,y_1) & .. & u_2'(x_p,y_1) & u_2'(x_1,y_2) & .. & u_2'(x_p,y_q) \\ : & : & .. & : & : & .. & : \\ : & : & .. & : & : & .. & : \\ u_N'(x_1,y_1) & u_N'(x_2,y_1) & .. & u_N'(x_p,y_1) & u_N'(x_1,y_2) & .. & u_N'(x_p,y_q) \end{bmatrix} = \begin{bmatrix} u_1'(X_1) & u_1'(X_2) & ... & u_1'(X_M) \\ u_2'(X_1) & u_2'(X_2) & ... & u_2'(X_M) \\ : & : & ... & : \\ : & : & ... & : \\ u_N'(X_1) & u_N'(X_2) & ... & u_N'(X_M) \end{bmatrix}. \tag{7}$$

Where $u_1'(X_2)$ is the value of u' at the spatial location X_2 in the 1^{st} snapshot and so on, We assume that velocity may be written as

$$U_i'(X_n) = \sum_{j=1}^{N} a_{ij}\phi_j(X_n). \tag{8}$$

Here, $\phi_j(X_n)$ is the j^{th} eigenfunction (or mode) and a_{ij} is the coefficient of the of the j^{th} mode that corresponds to the i^{th} snapshot of the velocity field. The goal is to prescribe a condition that would allow us to identify flow structures within a mode ϕ_j. The condition that achieves this, following Berkooz et al.,[20] is that the decomposition be optimal. Optimal here means that for a given number of modes, the decomposition will contain the most kinetic energy possible out of all possible decompositions. When this condition is met, the decomposition in Eq. (8) will represent the proper orthogonal decomposition. To impose the optimality condition, the Fredholm integral eigenvalue problem must be solved,

$$\int_{\Omega} R_{mn}\phi_j(X_n)d\Omega = \overline{\lambda}\phi_j(X_m). \tag{9}$$

Here, m is a free index, $\overline{\lambda}$ is the eigenvalue of mode j and Ω is the region of integration, which is the flow field space. R is the two-point correlation tensor defined as,

$$R_{mn} = \overline{u'(X_m)u'(X_n)} \tag{10}$$

To solve the eigenvalue problem, the integral in Eq. (9) must be approximated by a finite sum. This is accomplished by writing

$$\sum_{n=1}^{M} R_{mn}\phi_j(X_n)\Delta\Omega_n = \overline{\lambda}\phi_j(X_m). \tag{11}$$

Here, we have divided the domain into M subdivisions, each of size $\Delta\Omega_n$. Each subdivision encompasses a spatial (measurement) location X_n. To solve the eigenvalue problem in MATLAB, the matrix R can be constructed from U' as,

$$R = \frac{1}{N}U'^{T}U' \tag{12}$$

and the superscript T denotes the matrix transpose. The dimensions of R are $M \times M$. Using this, the eigenvalue problem of Eq. (11) can be written as,

$$R\overline{W}\phi_j = \overline{\lambda}\phi_j. \tag{13}$$

Here $\overline{W}$ is a diagonal matrix of dimensions $M \times M$ which contains the $\Delta\Omega_n$ values for all the spatial locations. From $\overline{W}$ can can extract a constant $\Delta\Omega$ and can write the eigenvalue problem as,

$$\Delta\Omega RW\phi_j = \overline{\lambda}\phi_j. \tag{14}$$

Now W contains the spatial weights of each location relative to the constant $\Delta\Omega$ and has no units. Furthermore, we can combine $\Delta\Omega$ with the eigenvalue ($\lambda = \overline{\lambda}/\Delta\Omega$) to write,

$$RW\phi_j = \lambda\phi_j. \tag{15}$$

Note that the eigenvalue λ has units of $\mathrm{m}^2\mathrm{s}^{-2}$. Eq. (15) represents the general eigenvalue problem and can be solved once W is determined. In the case of this work, the laser lines are evenly spaced except at two locations in the flow field. These locations correspond to the missing velocity profiles because of the gap in the microlens array. Therefore the spatial points in the two laser lines adjacent to the missing line have to be weighted by a factor of 1.5 more than all the other points in order to integrate over the entire domain. However it was found that, by neglecting the different spatial weights of the aforementioned points, the changes in the results were negligible, therefore in this work W was the identity matrix and the eigenvalue problem further simplifies to,

$$R\phi_j = \lambda\phi_j. \tag{16}$$

The dimensions of R are $M \times M$, which in this work is $\approx 2500\times2500$. This a fairly large matrix whose eigenvalue computation is expensive. To address this computational cost, Sirovitch[96] suggested solving the following nominally equivalent eigenvalue problem,

$$Ce_j = \lambda e_j. \tag{17}$$

Where $C = (1/N)U'U'^T$, with dimensions of $N \times N$ and e_j is the eigenvector. In this work $N \approx 900$ and therefore Eq. (17) is significantly much less computationally expensive than Eq. (16). The POD modes can be derived from Eq. (17) as,[97]

$$\phi_j = \frac{1}{\lambda_j N}\sum_{i=1}^{N} a_{ij}U'_i. \tag{18}$$

Where the coefficients a_{ij} are,

$$a_{ij} = e_{ij}\sqrt{\lambda_j N}. \tag{19}$$

The POD modes form an orthonormal set and are normalized such that,

$$< \phi_i \cdot \phi_j >= \delta_{ij}, \tag{20}$$

where δ_{ij} is the Kronecker delta and the angled brackets denote spatial integration. The eigenvalues have special significance because,

$$E_{tot} = \frac{1}{N}\sum_{i=1}^{N} < U'_i \cdot U'_i >= \sum_{j=1}^{N} \lambda_j \tag{21}$$

Consequently, each eigenvalue represents the contribution of its corresponding mode to the total energy, and in the discussion of results, the energies (λ_j), will be normalized by this E_{tot}.

VIII. Eigenvalues of Snapshot POD Analysis

In this section, we present and discuss the eigenvalue results from applying the snapshot POD method to the KTV data reported in earlier sections. In Fig. 15 (left), we present the cumulative fractional energy versus mode number. For each case, the first mode accounts for $\approx 20-30\%$ of the E_{tot} (Eq. (21)) and the first 6-10 modes capture approximately 60% of the E_{tot} in the flow. No clear trends as to the fraction of energy of the first mode or the cumulative fractional energy can be found between the different flow fields investigated in this work.

The eigenvalue spectrum is plotted for each case in Fig. 15 (right). Knight and Sirovitch[98] and Moser[99] suggest that the POD eigenfunctions are a good set of basis functions with which to form an inertial-range spectrum for inhomogeneous, turbulent flows, as is the case here. The famous inertial-range scaling due to Kolmogorov[100] is

$$E \propto \epsilon^{2/3} k^{-5/3} \tag{22}$$

where E is the energy per scalar wavenumber, ϵ is the dissipation rate, and k is the wavenumber. Stated equivalently

$$\mathscr{E} \propto \epsilon^{2/3} k^{-11/3}, \tag{23}$$

where $\mathscr{E}$ is the energy per vector wavenumber. Knight and Sirovitch[98] argue that the wave number is proportional to the mode number as $k \propto j^{1/3}$, and so in the inertial range the eigenvalues scale as

$$\lambda_j \propto j^{-11/9}, \tag{24}$$

which is represented in Fig. 15 (right) as a dashed line. Knight and Sirovitch[98] also state that the inertial range will be shorter by a factor of three in equivalent wave number space (measured in decades). The differences between the different spectra presented here are modest for mode numbers $j < 100$, above which the noise from the measurement technique may play a role.

The similarity between the spectra is somewhat surprising considering how dissimilar and inhomogeneous each case is. The authors initially expected an appreciably different eigenvalue spectrum in the flow between say the 32° corner flow, which is inhomogeneous in the streamwise and wall-normal directions and has a relatively large separated region, and boundary-layer flow, which is attached and inhomogeneous in only the wall-normal direction. However, upon close inspection, the first few POD modes do not clearly scale as $j^{-11/9}$, and these modes contain the structures (inhomogeneity and separation) which strongly modify the mean flow; this will be evident in the forthcoming presentation of the POD modes.

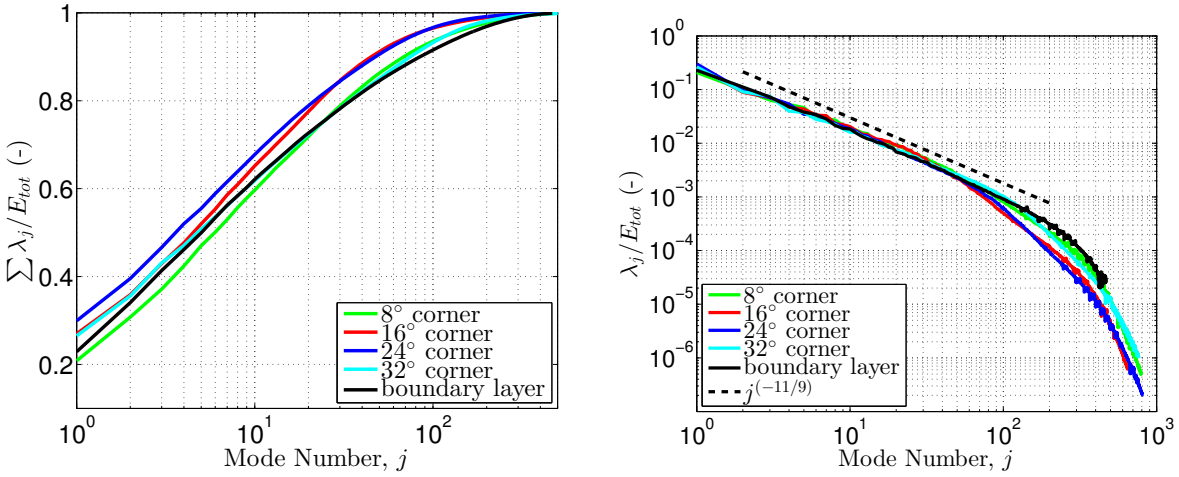

Figure 15: *Left:* The cumulative fraction of energy, $\sum \lambda_j/E_{tot}$. *Right:* The fraction of energy of each mode, λ_j/E_{tot}. The black line is the mode number raised to the (-11/9) power as suggested in Knight and Sirovitch[98]

.

This scaling of the eigenvalues is similar to that found in Piponniau et al.[29] where a POD analysis was performed on PIV results from an induced-shock-wave/turbulent boundary-layer interaction. Piponniau et al.[29] report a smaller observed value of the rolloff ($\lambda \propto j^{-0.9}$) which may be due to the fact that: 1) the flow field is not the same (impinged-shock/boundary-layer interaction vs. corner flow); 2) it is understood that the wall-normal component of fluctuating velocity tends to have a flatter spectrum in high-speed wall-bounded boundary layers than does the streamwise component[83] and Piponniau et al.[29] utilized both streamwise and wall-normal velocities in their analysis vs. only streamwise in the present analyis; and 3) the measurement technique was PIV in Piponniau et al.[29] vs. KTV in the present work.

IX. POD Coefficients and Modes of 24-degree Corner Flow

Here, we will discuss the 24° corner flow case in detail because it is often explored in other literature. In Fig. 16 (left), we present the first POD mode coefficients, $a_{i1}/\sqrt{E_{tot}}$ for the 24° corner flow. We do not observe any clear trends in time for this or any POD mode. Additionally, we do not observe any clear phenomena when constructing phase portraits (two different POD mode coefficients plotted against one another), or transforming the POD mode coefficients into frequency space. The laser repetition rate for this experiment is fixed to 10 Hz dictating a Nyquist frequency of 5 Hz; this repetition rate is not high enough to capture the unsteadiness observed and discussed in the literature.[101]

The sample distribution of energy for the first POD mode of the 24° corner flow is presented in Fig. 16 (right). There are no observable biases about the mean to within experimental error. Also in this figure, we mark the locations corresponding to 1.5 standard deviations (1.5σ) of the $|a_{i1}|$ samples which have the largest magnitude; we will use the samples that correspond to these large coefficient values (positive and negative) to gain insight into the mean-flow behavior exhibited by the POD modes.

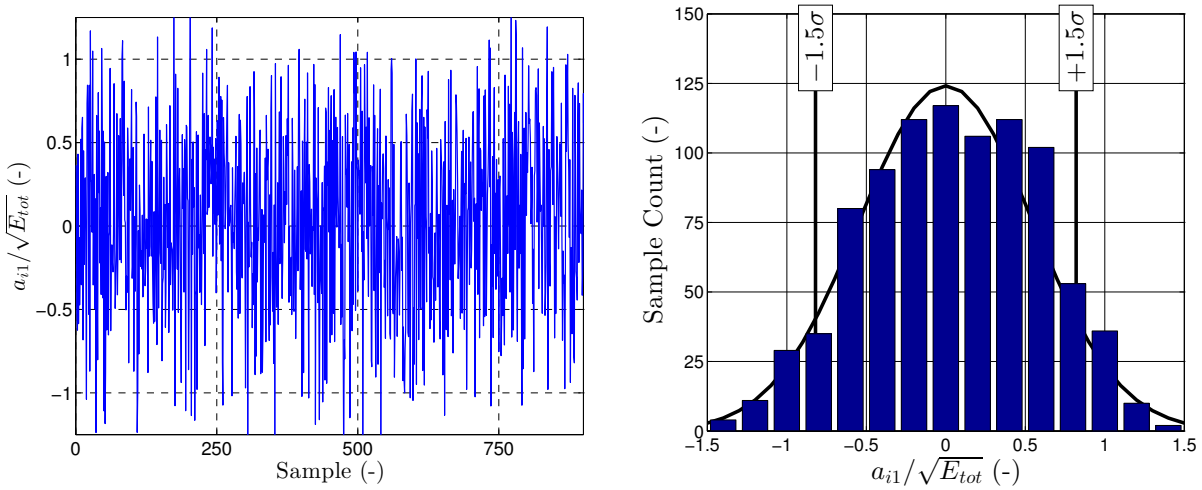

Figure 16: First POD mode coefficients for 24° corner flow. Left: Coefficients for POD mode $j = 1$, a_{i1} vs. sample number. Right: Sample distribution of coefficients for mode $j = 1$. Vertical black bars mark 1.5 standard deviations (1.5σ) indicating large magnitude coefficients $|a_{i1}|$.

The first six POD modes for the 24° corner flow are shown as contours of ϕ_j in the first row of Fig. 17. To illustrate the effect of the different POD modes on the mean-flow, the mean streamwise velocity of snapshots that correspond to the largest positive and negative mode coefficients is presented in the second and third rows of Fig. 17, respectively. That is, in the second row of Fig. 17, we present the mean of the streamwise velocity of the snapshots corresponding to samples falling above 1.5 standard deviations of the POD mode coefficient distribution ($+1.5\sigma$ of a_{i1}). And, in the third row of Fig. 17, we present the mean of the streamwise velocity of the snapshots corresponding to samples falling below 1.5 standard deviations of the POD mode coefficient distribution (-1.5σ of a_{i1}).

The first POD mode, ϕ_1, of the 24° corner flow case appears in the first row of the first column in Fig. 17. Inspecting the mean velocity field associated with large values of the mode coefficients, it appears that this

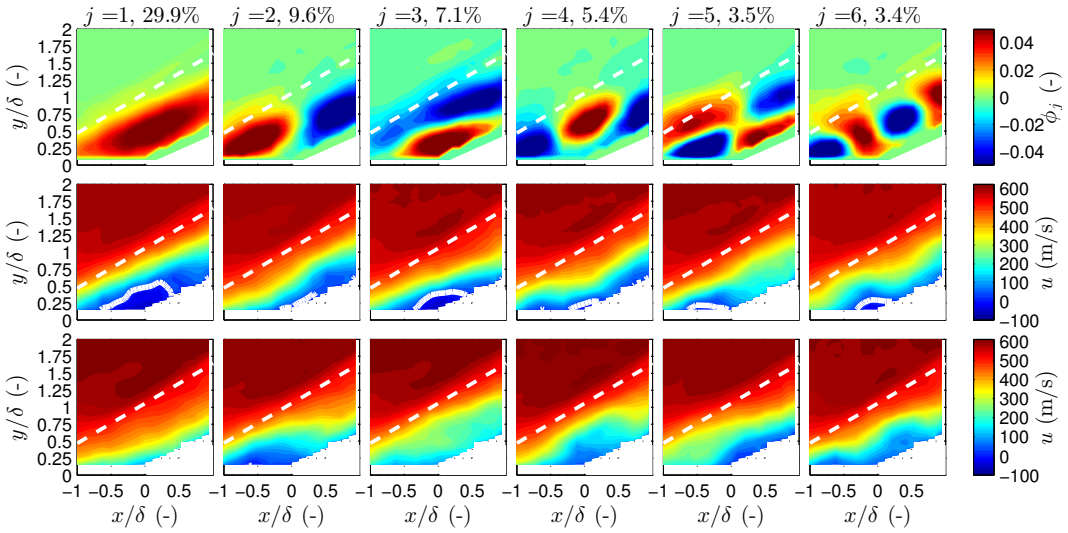

Figure 17: Snapshot POD analysis for the 24° corner flow. Each column corresponds to one of the first six POD modes marked by the mode number j and the fraction of energy associated with each mode in %. Top row: POD modes for the 24° corner flow are shown as contours of ϕ_j. Middle row: the mean streamwise velocity of snapshots with the largest positive mode coefficients (samples falling to right of $+1.5\sigma$ in in Fig. 16). Bottom row: the mean streamwise velocity of snapshots with the largest negative mode coefficients (samples falling to left of -1.5σ in in Fig. 16). A solid white line denotes the boundary between positive and negative streamwise velocity. A dashed white line denotes the mean shock location.

POD mode is associated with large-scale filling ($+1.5\sigma$ of a_{i1}, second row, first column of Fig. 17) and complete collapse (-1.5σ of a_{i1}, third row, first column of Fig. 17) of the separation bubble at the root of the corner. The second POD mode, (ϕ_2, second column of first row) appears to be the separation bubble oscillating in the streamwise direction as evidenced by the POD mode and the associated mean velocity fields associated with the large mode coefficients ($\pm 1.5\sigma$ of a_{i2}). It appears that there is a sloshing, or shift in the streamwise direction of high and low momentum fluid. The third POD mode (ϕ_3, third column of first row) appears to be smaller-scale separation-bubble filling and collapse in comparison with ϕ_1. There is an additional flow feature: when the flow is separated, there is a momentum surplus in the region immediately above the separation location and when the separation bubble is collapsed, there is a momentum deficit in the same region. This is potentially indicative of snapshots where the separation bubble is in the process of filling or collapsing. Modes ϕ_4 and ϕ_5 (fourth and fifth column of first row, respectively) appear to be harmonics of modes ϕ_2 and ϕ_3, respectively. Mode ϕ_6 (sixth column of first row, respectively) is difficult to interpret, but could be a harmonic of ϕ_4. Higher order modes, not pictured here, indicate increasingly smaller structures within the boundary layer and shock layer. In some of the higher modes, there are thin structures which appear close to the mean shock location, but these structures are associated with POD modes containing less than 1% of the TKE in the flow. That is, the energy associated with fluctuations from the mean-shock location are small relative to the fluctuations associated with the dynamics of the separation bubble.

X. Comparison of POD Analyses Between Cases

The POD analysis applied to the 24° corner case that was presented in Fig. 17 is also applied to the 8° corner, 16° corner, 32° corner and boundary-layer cases and presented in Figs. 20, 21, 22 and 23, respectively.

Several characteristics of the POD analyses are common among each of the cases. For all cases, the POD modes only register interesting content within the boundary layer and shock layer. This is a sensible result as the freestream disturbances are small and incoherent relative to the disturbances within the shock and boundary layers. For mode number higher than approximately $j = 10$, the POD modes are difficult to distinguish from one case to another, besides the obvious change in boundary geometry. That is, the

disturbances evident in the high order POD modes appear quite similar between cases in terms of distribution, amplitude, and length scale. To illustrate this point, POD mode ϕ_{30} is presented in Fig. 18 for each of the cases. The qualitative observation of commonality of the higher POD modes is also evident in the spectra of the eigenvalues presented in Fig. 15 (right). The initial thought was that the commonality of the higher order modes was due to noise in the measurement technique, which is also common among all cases. However, the signal-to-noise ratio appears sufficient at high mode number (Fig. 18).

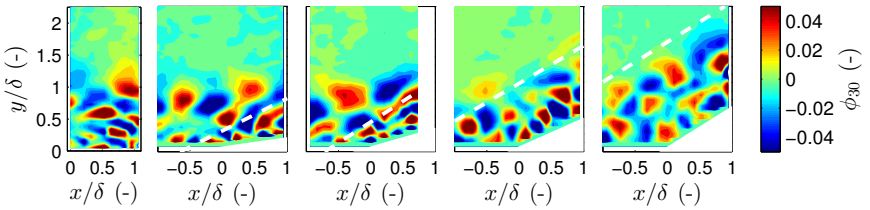

Figure 18: Comparison of POD mode ϕ_{30} among the boundary-layer and 8°, 16°, 24°, and 32° corner flows, from left to right, respectively. A dashed white line denotes the mean shock location.

Several characteristics of the POD analyses are dissimilar between the cases. In contrast to the 16°, 24° and 32° corner cases, the first POD of the 8° corner does not appear to indicate a relatively large separation bubble. It is also clear in the 24° and 32° cases that the shock layer plays a clear role in determining the length scale of the boundary of the disturbances. The fitting of an ellipse to the first POD mode was used to estimate length scales. The equation of an ellipse (with a schematic in Fig. 19 (left)) centered around x_0 and y_0 and rotated by an angle θ_{st} with respect to the x axis is

$$\frac{(x-x_0)\cos(\theta_{st})+(y-y_0)\sin(\theta_{st})}{a^2}+\frac{(y-y_0)\cos(\theta_{st})+(x-x_0)\sin(\theta_{st})}{b^2}=1, \tag{25}$$

where a and b are the semimajor and semiminor axes, respectively. The values of the parameters a, b, x_0, y_0 and θ_{st} were determined using the least-squares method of fitting. Using an ellipse as a curve of best fit for the first POD mode is justified as: 1) the structures appear elliptical in nature; and, 2) it gives values for three physical properties of the structures: the angle (θ_{st}), the length ($L_1 = 2a$), and the thickness ($L_2 = 2b$).

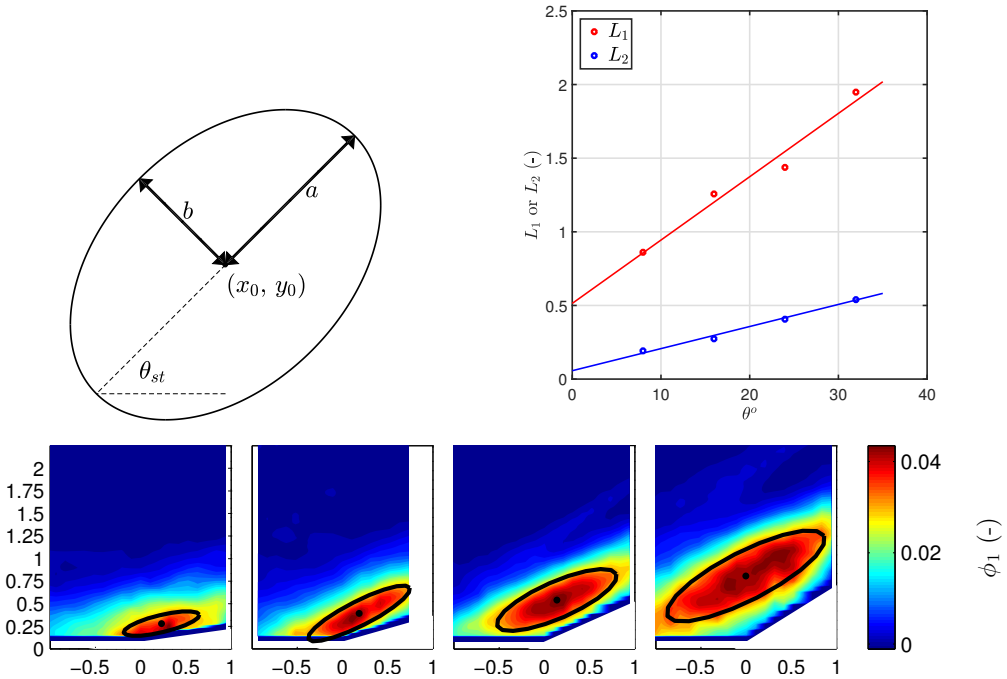

Figure 19: *Top:* Geometry of elliptical fit to structures (left) and the scaling of the length scales with wedge angles (right). The non-dimensional length L_1 is $2a$, and the non-dimensional thickness L_2 is $2b$. *Bottom:* Overlay of elliptical fit to the first POD mode for the 8, 16, 24 and 32 degree corners respectively.

The elliptical fits to the first POD mode for the four corners are shown in Fig. 19 (bottom) along with the plot of the two length scales L_1 and L_2 vs. corner angle (top right). The scaling relations for L_1 and L_2 with respect to θ are shown in Table 4. The relations show that L_1 and L_2 scale at different rates and that the scaling for both is linear with respect to the corner angle. No trends were observed for the structure angle θ_{st}.

Table 4: Sclaing relations for POD mode 1 structures.

Length scale (-)	Fit
L_1	$0.043\theta + 0.514$
L_2	$0.015\theta + 0.057$

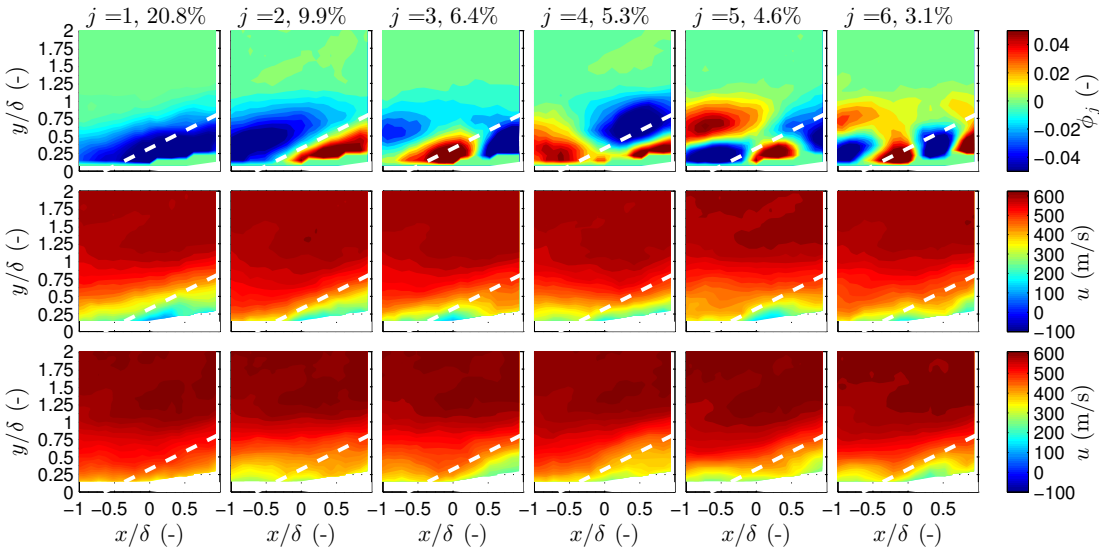

Figure 20: Snapshot POD analysis for the 8° corner flow. Top row: POD modes are shown as contours of ϕ_j. Middle and bottom row: the mean streamwise velocity of snapshots that correspond to the largest positive and negative mode coefficients, respectively. A dashed white line denotes the mean shock location.

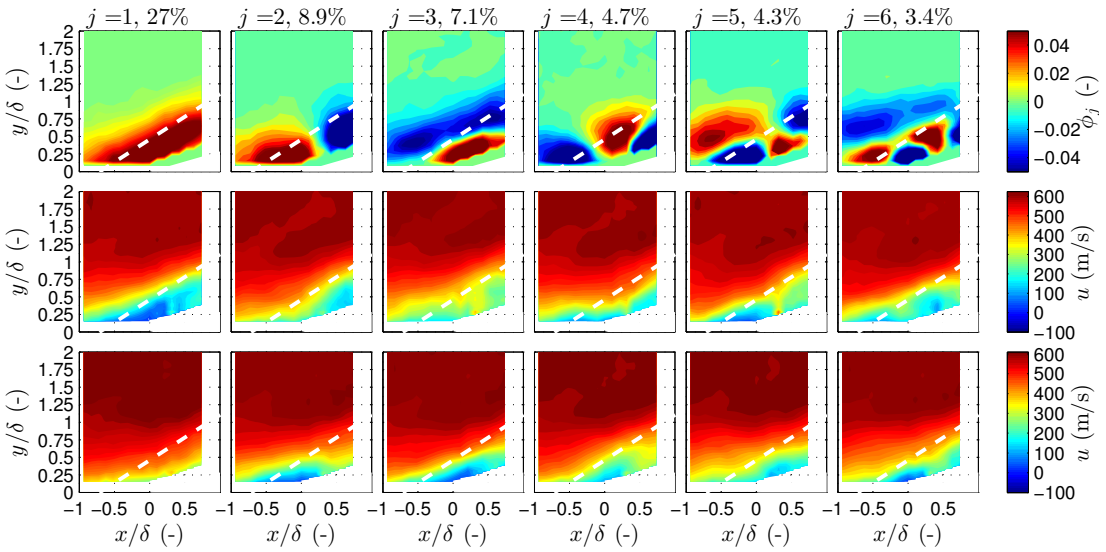

Figure 21: Snapshot POD analysis for the 16° corner flow. Top row: POD modes are shown as contours of ϕ_j. Middle and bottom row: the mean streamwise velocity of snapshots that correspond to the largest positive and negative mode coefficients, respectively. A dashed white line denotes the mean shock location.

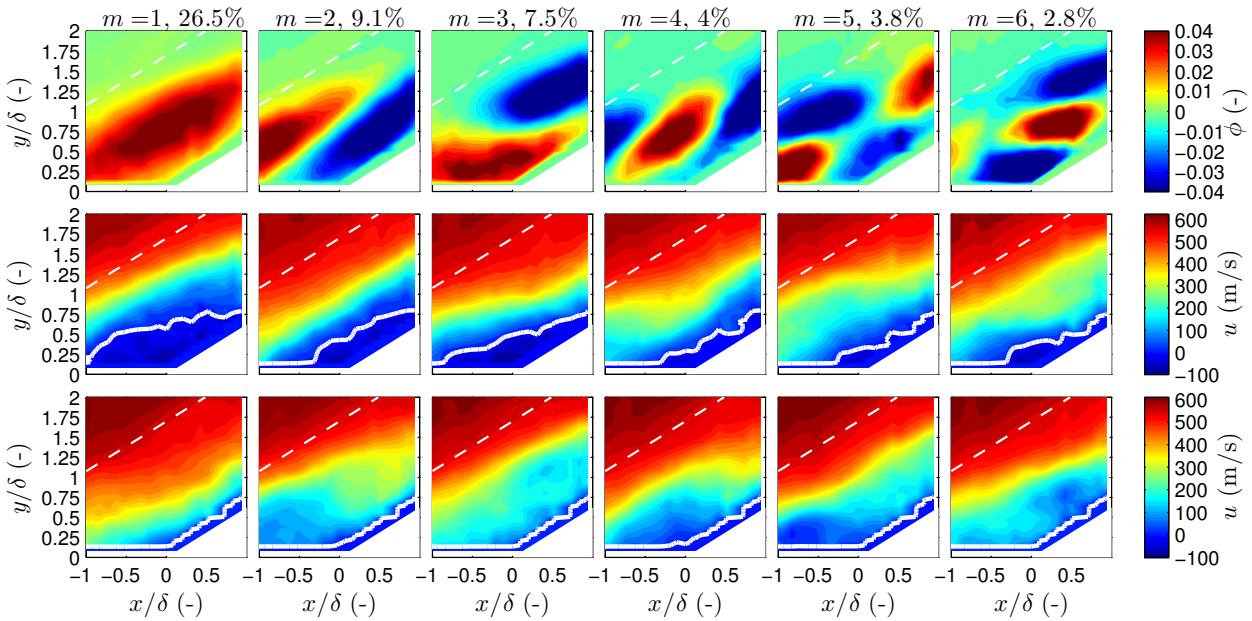

Figure 22: Snapshot POD analysis for the 32° corner flow. Top row: POD modes are shown as contours of ϕ_j. Middle and bottom row: the mean streamwise velocity of snapshots that correspond to the largest positive and negative mode coefficients, respectively. A dashed white line denotes the mean shock location.

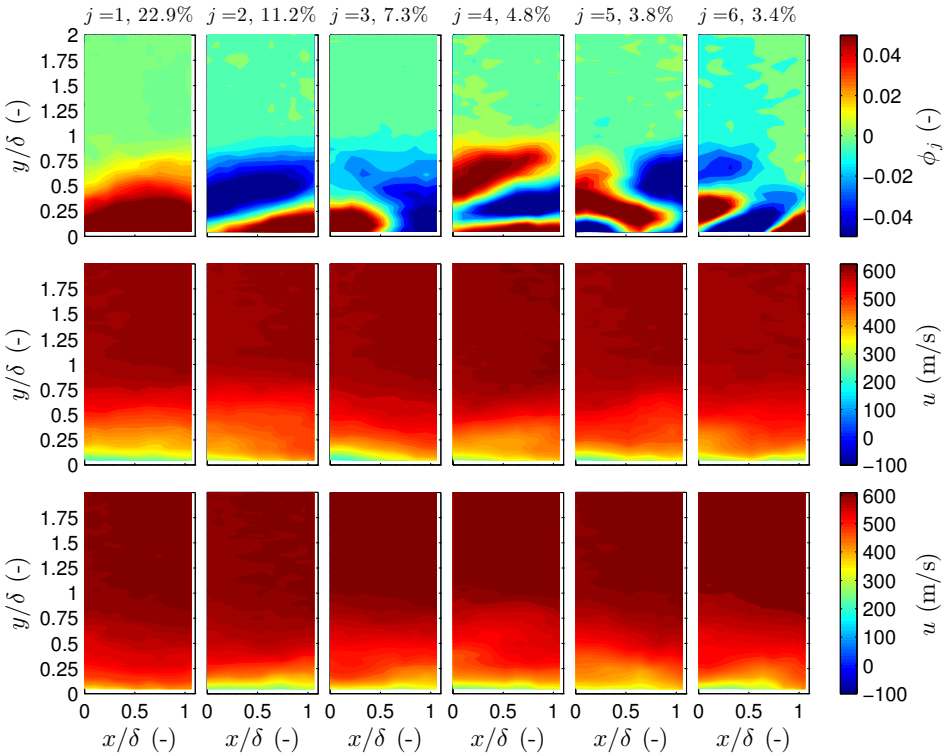

Figure 23: Snapshot POD analysis for the boundary-layer flow. Each column corresponds to one of the first six POD modes marked by the mode number j and the fraction of energy associated with each mode in %. Top row: POD modes are shown as contours of ϕ_j. Middle and bottom row: the mean streamwise velocity of snapshots that correspond to the largest positive and negative mode coefficients, respectively.

XI. Conclusions

The incoming boundary layer and shock-wave boundary-layer interaction over four compression corners at $M_\infty = 2.8$ were investigated using one-dimensional KTV in the M3CT. The focus of this study was the effect of compression-corner angle on streamwise turbulent kinetic energy (sTKE) and structure in Mach 2.8 flow. For example, this canonical flow may be observed in practice as the deflection of a control surface on a vehicle in high-speed flight or in the flow path of a high-speed, air-breathing engine.

For the incoming boundary layer, data from ten mean- and fluctuating-velocity profiles spanning ≈ 11 mm or $x/\delta \approx 1.1$ in the streamwise direction were reduced and compared to data from the literature. These comparisons included Van Direst scaling, Morkovin scaling of the streamwise velocity fluctuations, and longitudinal correlations. Comparisons are favorable between the KTV data collected in this work and experimental and computational data from the literature. From this, we concluded that the incoming flow could be nominally treated as a canonical, supersonic turbulent boundary layer and investigations of shock-wave/turbulent boundary-layer interactions could commence.

Typical Z-type schlieren images were recorded for each compression-corner flow to address concerns about potential tunnel-starting issues in the M3CT. We found no such tunnel-starting issues and made fits to the mean initial shock-wave angle, which also favorably compared to data in the literature, thus building confidence in studing these geometries in the M3CT.

For the shock-wave/turbulent boundary-layer interactions, data from ≈20 mean- and fluctuating-velocity profiles spanning ≈ 22 mm or $x/\delta \approx 2.1$ were recorded for compression-corner angles of 8, 16, 24, and 32 degrees. This was an effective demonstration of extending the application of tagging velocimetry into a complex flow field.

For the 16, 24, and 32 degree cases, the shear layer near the root of interaction region was identified and a coordinate system was fitted the the maxima of sTKE ($u'^2_{RMS}/(U^2_2)$). Although sTKE in the lab frame was used because the present KTV measurements were one dimensional (as opposed to Helm et al.,[95] where the calculations were two dimensional), we found that the resulting sTKE profiles were self similar.

In an effort to identify trends of longitudinal turbulent stress with compression corner angle, we defined a figure of merit termed the wall-normal integrated mean sTKE, $\overline{\text{sTKE}}$. This figure of merit is intended to identify the overall longitudinal turbulent stress contained in the flow at different x/δ locations which should be relatively easy to compare between other experimental and computational studies. Because $\overline{\text{sTKE}}$ is the wall-normal integrated mean, it will capture the amplitude of $u'^2_{RMS}/(2U^2_\infty)$, in addition to the effect of the width of the shear layer in each case. We observe that the wall-normal integrated mean sTKE ($\overline{\text{sTKE}}$) scales as an exponential with respect to the compression-corner angle.

POD was applied to the KTV data to examine the structures in the flow for each case. To identify the modification of the mean flow due to each POD mode, we present the mean streamwise velocity of the samples which correspond to the POD mode coefficients falling above and below 1.5 standard deviations ($\pm 1.5\sigma$ of a_{ij}). We observed that the first several modes are somewhat similar between each compression corner case (with the exception of the 8-degree corner). These first POD modes contain most of the kinetic energy and are those that modify the mean flow giving rise to such features as separation bubble filling/collapse and oscillation.

Knight and Sirovitch[98] and Moser[99] suggest that the POD eigenfunctions are a good set of basis functions with which to form an inertial-range spectrum for inhomogeneous, turbulent flows, and such a spectrum was identified in this work. That is, we found the POD eigenspectra to scale as $\lambda_j \propto j^{-11/9}$ which is analogous to the famous inertial-range scaling due to Kolmogorov[100] ($E \propto \epsilon^{2/3} k^{-5/3}$). At POD mode number greater than ≈ 10 there was an initially unanticipated similarity between the eigenspectra considering how dissimilar and inhomogeneous each case is. We initially expected an appreciably different eigenvalue spectrum in the flow between say the 32° corner flow, which is inhomogeneous in the streamwise and wall-normal directions and has a relatively large separated region, and boundary-layer flow, which is attached and inhomogeneous in only the wall-normal direction. However, upon close inspection, the first few POD modes do not clearly scale as $j^{-11/9}$, and these modes contain the structures (inhomogeneity and separation) which strongly modify the mean flow. Following the first ≈ 10 modes, the similarity of the inertial range is apparent between each case.

Acknowledgments

The M3CT facilities were supplied by the Arnold Engineering Development Complex (AEDC). The Air Force Summer Faculty Fellowship Program (SFFP) supported Mustafa and Parziale with a stipend for this work. Mustafa and Parziale were supported by AFOSR Young Investigator Program Grant FA9550-16-1-0262 and equipment for this work was supported by AFOSR DURIP Grant FA9550-15-1-0325; Ivett Leyva of AFOSR is the Program Manager for both grants. We acknowledge the machine work done by Milan Simonovic and Marshall Reid of Stevens Institute of Technology. We also would like to thank Jonathan Brooks of University of Maryland for assistance with operating the wind tunnel and the Pitot measurements. We would like to acknowledge the encouragement of John Laffery and Dan Marren of AEDC White Oak.

References

[1]Dolling, D. S., "Fifty Years of Shock-Wave/Boundary-Layer Interaction Research: What next?" *AIAA Journal*, Vol. 39, No. 8, 2001, pp. 1517–1531. doi: 10.2514/2.1476.

[2]Wang, B., Sandham, N. D., Hu, Z., and Liu, W., "Numerical study of oblique shock-wave/boundary-layer interaction considering sidewall effects," *Journal of Fluid Mechanics*, Vol. 767, 2015, pp. 526–561. doi: 10.1017/jfm.2015.58.

[3]John, B., Kulkarni, V. N., and Natarajan, G., "Shock wave boundary layer interactions in hypersonic flows," *International Journal of Heat and Mass Transfer*, Vol. 70, 2014, pp. 81–90. doi: 10.1016/j.ijheatmasstransfer.2013.10.072.

[4]Adams, N. A., "Direct simulation of the turbulent boundary layer along a compression ramp at $M = 3$ and $Re_\Theta = 1685$," *Journal of Fluid Mechanics*, Vol. 420, 2000, pp. 47–83. doi: 10.1017/S0022112000001257.

[5]Wu, M. and Martin, M. P., "Direct Numerical Simulation of Supersonic Turbulent Boundary Layer Over a Compression Ramp," *AIAA Journal*, Vol. 45, No. 4, 2007, pp. 879–889. doi: 10.2514/1.27021.

[6]Wu, M. and Martin, M. P., "Analysis of shock motion in shockwave and turbulent boundary layer interaction using direct numerical simulation data," *Journal of Fluid Mechanics*, Vol. 594, 2008, pp. 71–83. doi: 10.1017/S0022112007009044.

[7]Giepman, R. H. M., Schrijer, F. F. J., and van Oudheusden, B. W., "High-resolution PIV measurements of a transitional shock wave-boundary layer interaction," *Experiments in Fluids*, Vol. 56, No. 6, 2015, pp. 113. doi: 10.1007/s00348-015-1977-8.

[8]Settles, G. S., Vas, I. E., and Bogdonoff, S. M., "Details of a Shock-Separated Turbulent Boundary Layer at a Compression Corner," *AIAA Journal*, Vol. 14, No. 12, 1976, pp. 1709–1715. doi: 10.2514/3.61513.

[9]Settles, G. S., Fitzpatrick, T. J., and Bogdonoff, S. M., "Detailed Study of Attached and Separated Compression Corner Flowfields in High Reynolds Number Supersonic Flow," *AIAA Journal*, Vol. 17, No. 6, 1979, pp. 579–585. doi: 10.2514/3.61180.

[10]Smits, A. J. and Muck, K.-C., "Experimental study of three shock wave/turbulent boundary layer interactions," *Journal of Fluid Mechanics*, Vol. 182, 1987, pp. 291–314. doi: 10.1017/S0022112087002349.

[11]Humble, R. A., Scarano, F., and van Oudheusden, B. W., "Particle image velocimetry measurements of a shock wave/turbulent boundary layer interaction," *Experiments in Fluids*, Vol. 43, No. 2-3, 2007, pp. 173–183. doi: 10.1007/s00348-007-0337-8.

[12]Humble, R. A., Elsinga, G. E., Scarano, F., and van Oudheusden, B. W., "Three-dimensional instantaneous structure of a shock wave/turbulent boundary layer interaction," *Journal of Fluid Mechanics*, Vol. 622, 2009, pp. 33–62. doi: 10.1017/S0022112008005090.

[13]Gaitonde, D. V., "Progress in shock wave/boundary layer interactions," *Progress in Aerospace Sciences*, Vol. 72, 2015, pp. 80–99. doi: 10.1016/j.paerosci.2014.09.002.

[14]Settles, G. S. and, D. L. J., "Hypersonic Shock/Boundary-Layer Interaction Database: New and Corrected Data," NASA CR 177638, 1994.

[15]Knight, D., Yan, H., Panaras, A. G., and Zheltovodov, A., "Advances in CFD prediction of shock wave turbulent boundary layer interactions," *Progress in Aerospace Sciences*, Vol. 39, No. 2, 2003, pp. 121–184. doi: 10.1016/S0376-0421(02)00069-6.

[16]Babinsky, H. and Harvey, J. K., editors, *Shock Wave-Boundary-Layer Interactions*, Cambridge University Press, 1st ed., 2011.

[17]Porter, K. M. and Poggie, J., "Turbulent Structure and Large-Scale Unsteadiness in Shock-Wave/Boundary Layer Interaction," *Proceedings of AIAA SciTech 2017*, AIAA-2017-0533, Grapevine, Texas, 2017. doi: 10.2514/6.2017-0533.

[18]Tennekes, H. and Lumley, J. L., *A First Course in Turbulence*, MIT press, 1972.

[19]Lumley, J. L., "The structure of inhomogeneous turbulent flows," *Atmospheric Turbulence and Radio Wave Propagation*, edited by A. M. Yaglom and V. I. Tatarsky, 1967, pp. 166–176.

[20]Berkooz, G., Holmes, P., and Lumley, J. L., "The Proper Orthogonal Decomposition in the Analysis of Turbulent Flows," *Annual Review of Fluid Mechanics*, Vol. 25, No. 1, 1993, pp. 539–575. doi: 10.1146/annurev.fl.25.010193.002543.

[21]Taira, K., Brunton, S. L., Dawson, S. T. . M., Rowley, C. W., Colonius, T., McKeon, B. J., Schmidt, O. T., Gordeyev, S., Theofilis, V., and Ukeiley, L. S., "Modal Analysis of Fluid Flows: An Overview," *AIAA Journal*, 2017, pp. 1–29. doi: 10.2514/1.J056060.

[22]Chen, H., Reuss, D. L., and Sick, V., "On the use and interpretation of proper orthogonal decomposition of in-cylinder engine flows," *Measurement Science and Technology*, Vol. 23, No. 8, 2012, pp. 085302. doi: 10.1088/0957-0233/23/8/085302.

[23]Chen, H., Reuss, D. L., Hung, D. L., and Sick, V., "A practical guide for using proper orthogonal decomposition in engine research," *International Journal of Engine Research*, Vol. 14, No. 4, 2013, pp. 307–319. doi: 10.1177/1468087412455748.

[24]Druault, P., Guibert, P., and Alizon, F., "Use of proper orthogonal decomposition for time interpolation from PIV data," *Experiments in Fluids*, Vol. 39, No. 6, Dec 2005, pp. 1009–1023. doi: 10.1007/s00348-005-0035-3.

[25]Orellano, A. and Wengle, H., "POD analysis of coherent structures in forced turbulent flow over a fence," *Journal of Turbulence*, Vol. 2, 2001, pp. N8. doi: 10.1088/1468-5248/2/1/008.

[26]Murray, N., Sllstrm, E., and Ukeiley, L., "Properties of subsonic open cavity flow fields," *Physics of Fluids*, Vol. 21, No. 9, 2009, pp. 095103. doi: 10.1063/1.3210772.

[27]Bonnet, J. P., Cole, D. R., Delville, J., Glauser, M. N., and Ukeiley, L. S., "Stochastic estimation and proper orthogonal decomposition: Complementary techniques for identifying structure," *Experiments in Fluids*, Vol. 17, No. 5, Sep 1994, pp. 307–314. doi: 10.1007/BF01874409.

[28]Tu, J. H., Rowley, C. W., Kutz, J. N., and Shang, J. K., "Spectral analysis of fluid flows using sub-Nyquist-rate PIV data," *Experiments in Fluids*, Vol. 55, No. 9, Sep 2014. doi: 10.1007/s00348-014-1805-6.

[29]Piponniau, S., Collin, E., Dupont, P., and Debiève, J., "Reconstruction of velocity fields from wall pressure measurements in a shock wave/turbulent boundary layer interaction," *International Journal of Heat and Fluid Flow*, Vol. 35, 2012, pp. 176–186. doi: 10.1016/j.ijheatfluidflow.2012.02.006.

[30]Zahradka, D., Parziale, N. J., Smith, M. S., and Marineau, E. C., "Krypton tagging velocimetry in a turbulent Mach 2.7 boundary layer," *Experiments in Fluids*, Vol. 57, No. 62, 2016. doi: 10.1007/s00348-016-2148-2.

[31]Mustafa, M. A., Hunt, M. B., Parziale, N. J., Smith, M. S., and Marineau, E. C., "Krypton Tagging Velocimetry (KTV) Investigation of Shock-Wave/Turbulent Boundary-Layer Interaction," *Proceedings of AIAA SciTech 2017*, AIAA-2017-0025, Grapevine, Texas, 2017. doi: 10.2514/6.2017-0025.

[32]Settles, G. S., *Schlieren and Shadowgraph Techniques*, Springer-Verlag Berlin Heidelberg, First ed., 2001.

[33]Spaid, F. W. and Frishett, J. C., "Incipient Separation of a Supersonic, Turbulent Boundary Layer, Including Effects of Heat Transfer," *AIAA*, Vol. 10, No. 7, 1972, pp. 915–922. doi: 10.2514/3.50245.

[34]Haertig, J., Havermann, M., Rey, C., and George, A., "Particle Image Velocimetry in Mach 3.5 and 4.5 Shock-Tunnel Flows," *AIAA Journal*, Vol. 40, No. 6, 2002, pp. 1056–1060. doi: 10.2514/2.1787.

[35]Loth, E., "Compressibility and Rarefaction Effects on Drag of a Spherical Particle," *AIAA Journal*, Vol. 46, No. 9, 2008, pp. 2219–2228. doi: 10.2514/1.28943.

[36]Hsu, A. G., Srinivasan, R., Bowersox, R. D. W., and North, S. W., "Molecular Tagging Using Vibrationally Excited Nitric Oxide in an Underexpanded Jet Flowfield," *AIAA Journal*, Vol. 47, No. 11, 2009, pp. 2597–2604. doi: 10.2514/1.39998.

[37]Hsu, A. G., Srinivasan, R., Bowersox, R. D. W., and North, S. W., "Two-component molecular tagging velocimetry utilizing NO fluorescence lifetime and NO_2 photodissociation techniques in an underexpanded jet flowfield," *Applied Optics*, Vol. 48, No. 22, 2009, pp. 4414–4423. doi: 10.1364/AO.48.004414.

[38]Sánchez-González, R., Srinivasan, R., Bowersox, R. D. W., and North, S. W., "Simultaneous velocity and temperature measurements in gaseous flow fields using the VENOM technique," *Optics Letters*, Vol. 36, No. 2, 2011, pp. 196–198. doi: 10.1364/OL.36.000196.

[39]Sánchez-González, R., Bowersox, R. D. W., and North, S. W., "Simultaneous velocity and temperature measurements in gaseous flowfields using the vibrationally excited nitric oxide monitoring technique: a comprehensive study," *Applied Optics*, Vol. 51, No. 9, 2012, pp. 1216–1228. doi: 10.1364/AO.51.001216.

[40]Sánchez-González, R., Bowersox, R. D. W., and North, S. W., "Vibrationally excited NO tagging by NO($A^2\Sigma^+$) fluorescence and quenching for simultaneous velocimetry and thermometry in gaseous flows," *Optics Letters*, Vol. 39, No. 9, 2014, pp. 2771–2774. doi: 10.1364/OL.39.002771.

[41]Dam, N., Klein-Douwel, R. J. H., Sijtsema, N. M., and ter Meulen, J. J., "Nitric oxide flow tagging in unseeded air," *Optics Letters*, Vol. 26, No. 1, 2001, pp. 36–38. doi: 10.1364/OL.26.000036.

[42]Sijtsema, N. M., Dam, N. J., Klein-Douwel, R. J. H., and ter Meulen, J. J., "Air Photolysis and Recombination Tracking: A New Molecular Tagging Velocimetry Scheme," *AIAA Journal*, Vol. 40, No. 6, 2002, pp. 1061–1064. doi: 10.2514/2.1788.

[43]Van der Laan, W. P. N., Tolboom, R. A. L., Dam, N. J., and ter Meulen, J. J., "Molecular tagging velocimetry in the wake of an object in supersonic flow," *Experiments in Fluids*, Vol. 34, No. 4, 2003, pp. 531–534. doi: 10.1007/s00348-003-0593-1.

[44]Miles, R., Cohen, C., Connors, J., Howard, P., Huang, S., Markovitz, E., and Russell, G., "Velocity measurements by vibrational tagging and fluorescent probing of oxygen," *Optics Letters*, Vol. 12, No. 11, 1987, pp. 861–863. doi: 10.1364/OL.12.000861.

[45]Miles, R., Connors, J., Markovitz, E., Howard, P., and Roth, G., "Instantaneous profiles and turbulence statistics of supersonic free shear layers by Raman excitation plus laser-induced electronic fluorescence (RELIEF) velocity tagging of oxygen," *Experiments in Fluids*, Vol. 8, No. 1-2, 1989, pp. 17–24. doi: 10.1007/BF00203060.

[46]Miles, R. B., Zhou, D., Zhang, B., and Lempert, W. R., "Fundamental Turbulence Measurements by RELIEF Flow Tagging," *AIAA Journal*, Vol. 31, No. 3, 1993, pp. 447–452. doi: 10.2514/3.11350.

[47]Miles, R. B. and Lempert, W. R., "Quantitative Flow Visualization in Unseeded Flows," *Annual Review of Fluid Mechanics*, Vol. 29, No. 1, 1997, pp. 285–326. doi: 10.1146/annurev.fluid.29.1.285.

[48]Miles, R. B., Grinstead, J., Kohl, R. H., and Diskin, G., "The RELIEF flow tagging technique and its application in engine testing facilities and for helium-air mixing studies," *Measurement Science and Technology*, Vol. 11, No. 9, 2000, pp. 1272–1281. doi: 10.1088/0957-0233/11/9/304.

[49]Michael, J. B., Edwards, M. R., Dogariu, A., and Miles, R. B., "Femtosecond laser electronic excitation tagging for quantitative velocity imaging in air," *Applied Optics*, Vol. 50, No. 26, 2011, pp. 5158–5162. doi: 10.1364/AO.50.005158.

[50]Edwards, M. R., Dogariu, A., and Miles, R. B., "Simultaneous Temperature and Velocity Measurements in Air with Femtosecond Laser Tagging," *AIAA Journal*, Vol. 53, No. 8, 2015, pp. 2280–2288. doi: 10.2514/1.J053685.

[51]Jiang, N., Halls, B. R., Stauffer, H. U., Danehy, P. M., Gord, J. R., and Roy, S., "Selective two-photon absorptive resonance femtosecond-laser electronic-excitation tagging velocimetry," *Optics Letters*, Vol. 41, No. 10, 2016, pp. 2225–2228. doi: 10.1364/OL.41.002225.

[52]Jiang, N., Mance, J. G., Slipchenko, M. N., Felver, J. J., Stauffer, H. U., Yi, T., Danehy, P. M., and Roy, S., "Seedless velocimetry at 100 kHz with picosecond-laser electronic-excitation tagging," *Optics Letters*, Vol. 42, No. 2, 2017, pp. 239–242. doi: 10.1364/OL.42.000239.

[53]Mills, J. L., *Investigation of Multi-Photon Excitation in Argon with Applications in Hypersonic Flow Diagnostics*, Ph.D. thesis, Old Dominion University, 2016.

[54]McDaniel, J. C., Hiller, B., and Hanson, R. K., "Simultaneous multiple-point velocity measurements using laser-induced iodine fluorescence," *Optics Letters*, Vol. 8, No. 1, 1983, pp. 51–53. doi: 10.1364/OL.8.000051.

[55]Balla, R. J., "Iodine Tagging Velocimetry in a Mach 10 Wake," *AIAA Journal*, Vol. 51, No. 7, 2013, pp. 1–3. doi: 10.2514/1.J052416.

[56]Barker, P., Bishop, A., and Rubinsztein-Dunlop, H., "Supersonic velocimetry in a shock tube using laser enhanced ionisation and planar laser induced fluorescence," *Applied Physics B*, Vol. 64, No. 3, 1997, pp. 369–376. doi: 10.1007/s003400050186.

[57]Lempert, W. R., Jiang, N., Sethuram, S., and Samimy, M., "Molecular Tagging Velocimetry Measurements in Supersonic Microjets," *AIAA Journal*, Vol. 40, No. 6, 2002, pp. 1065–1070. doi: 10.2514/2.1789.

[58]Lempert, W. R., Boehm, M., Jiang, N., Gimelshein, S., and Levin, D., "Comparison of molecular tagging velocimetry data and direct simulation Monte Carlo simulations in supersonic micro jet flows," *Experiments in Fluids*, Vol. 34, No. 3, 2003, pp. 403–411. doi: 10.1007/s00348-002-0576-7.

[59]Handa, T., Mii, K., Sakurai, T., Imamura, K., Mizuta, S., and Ando, Y., "Study on supersonic rectangular microjets using molecular tagging velocimetry," *Experiments in Fluids*, Vol. 55, No. 5, 2014, pp. 1–9. doi: 10.1007/s00348-014-1725-5.

[60]Zhang, S., Yu, X., Yan, H., Huang, H., and Liu, H., "Molecular tagging velocimetry of NH fluorescence in a high-enthalpy rarefied gas flow," *Applied Physics B*, Vol. 123, No. 4, 2017, pp. 122. doi: 10.1007/s00340-017-6703-1.

[61]Boedeker, L. R., "Velocity measurement by H_2O photolysis and laser-induced fluorescence of OH," *Optics Letters*, Vol. 14, No. 10, 1989, pp. 473–475. doi: 10.1364/OL.14.000473.

[62]Wehrmeyer, J. A., Ribarov, L. A., Oguss, D. A., and Pitz, R. W., "Flame Flow Tagging Velocimetry with 193-nm H_2O Photodissociation," *Applied Optics*, Vol. 38, No. 33, 1999, pp. 6912–6917. doi: 10.1364/AO.38.006912.

[63]Pitz, R. W., Lahr, M. D., Douglas, Z. W., Wehrmeyer, J. A., Hu, S., Carter, C. D., Hsu, K.-Y., Lum, C., and Koochesfahani, M. M., "Hydroxyl tagging velocimetry in a supersonic flow over a cavity," *Applied Optics*, Vol. 44, No. 31, 2005, pp. 6692–6700. doi: 10.1364/AO.44.006692.

[64]André, M. A., Bardet, P. M., Burns, R. A., and Danehy, P. M., "Characterization of hydroxyl tagging velocimetry for low-speed flows," *Measurement Science and Technology*, Vol. 28, No. 8, 2017, pp. 085202. doi: 10.1088/1361-6501/aa7ac8.

[65]Hiller, B., Booman, R. A., Hassa, C., and Hanson, R. K., "Velocity visualization in gas flows using laser-induced phosphorescence of biacetyl," *Review of Scientific Instruments*, Vol. 55, No. 12, 1984, pp. 1964–1967. doi: 10.1063/1.1137687.

[66]Gendrich, C. P. and Koochesfahani, M. M., "A spatial correlation technique for estimating velocity fields using molecular tagging velocimetry (MTV)," *Experiments in Fluids*, Vol. 22, No. 1, 1996, pp. 67–77. doi: 10.1007/BF01893307.

[67]Gendrich, C. P., Koochesfahani, M. M., and Nocera, D. G., "Molecular tagging velocimetry and other novel applications of a new phosphorescent supramolecule," *Experiments in Fluids*, Vol. 23, No. 5, 1997, pp. 361–372. doi: 10.1007/s003480050123.

[68]Stier, B. and Koochesfahani, M. M., "Molecular tagging velocimetry (MTV) measurements in gas phase flows," *Experiments in Fluids*, Vol. 26, No. 4, 1999, pp. 297–304. doi: 10.1007/s003480050292.

[69]Ribarov, L. A., Wehrmeyer, J. A., Batliwala, F., Pitz, R. W., and DeBarber, P. A., "Ozone Tagging Velocimetry Using Narrowband Excimer Lasers," *AIAA Journal*, Vol. 37, No. 6, 1999, pp. 708–714. doi: 10.2514/2.799.

[70]André, M. A., Burns, R. A., Danehy, P. M., Cadell, S. R., Woods, B. G., and Bardet, P. M., "Development of N_2O-MTV for low-speed flow and in-situ deployment to an integral effect test facility," *Experiments in Fluids*, Vol. 59, No. 1, 2018, pp. 14. doi: 10.1007/s00348-017-2470-3.

[71]Mills, J. L., Sukenik, C. I., and Balla, R. J., "Hypersonic Wake Diagnostics Using Laser Induced Fluorescence Techniques," *Proceedings of 42nd AIAA Plasmadynamics and Lasers Conference*, AIAA 2011-3459, Honolulu, Hawaii, 2011. doi: 10.2514/6.2011-3459.

[72]Balla, R. J. and Everhart, J. L., "Rayleigh Scattering Density Measurements, Cluster Theory, and Nucleation Calculations at Mach 10," *AIAA Journal*, Vol. 50, No. 3, 2012, pp. 698–707. doi: 10.2514/1.J051334.

[73]Parziale, N. J., Smith, M. S., and Marineau, E. C., "Krypton Tagging Velocimetry for Use in High-Speed Ground-Test Facilities," *Proceedings of AIAA SciTech 2015*, AIAA-2015-1484, Kissimmee, Florida, 2015. doi: 10.2514/6.2015-1484.

[74]Parziale, N. J., Smith, M. S., and Marineau, E. C., "Krypton tagging velocimetry of an underexpanded jet," *Applied Optics*, Vol. 54, No. 16, 2015, pp. 5094–5101. doi: 10.1364/AO.54.005094.

[75]Zahradka, D., Parziale, N. J., Smith, M. S., and Marineau, E. C., "Krypton Tagging Velocimetry (KTV) in Supersonic Turbulent Boundary Layers," *Proceedings of AIAA SciTech 2016*, AIAA-2016-1587, San Diego, California, 2016. doi: 10.2514/6.2016-1587.

[76]Mustafa, M. A., , and Parziale, N. J., "Krypton Tagging Velocimetry in the Stevens Shock Tube," *Proceedings of 33rd AIAA Aerodynamic Measurement Technology and Ground Testing Conference*, AIAA-2017-3897, Denver, Colorado, 2017. doi: 10.2514/6.2017-3897.

[77]Mustafa, M. A., Parziale, N. J., Smith, M. S., and Marineau, E. C., "Nonintrusive Freestream Velocity Measurement in a Large-Scale Hypersonic Wind Tunnel," *AIAA Journal*, Vol. 55, No. 10, 2017, pp. 3611–3616. doi: 10.2514/1.J056177.

[78]Mustafa, M. A., Parziale, N. J., Smith, M. S., and Marineau, E. C., "Two-Dimensional Krypton Tagging Velocimetry (KTV-2D) Investigation of Shock-Wave/Turbulent Boundary-Layer Interaction," *Proceedings of AIAA SciTech 2018*, AIAA-2018-1771, Kissimmee, Florida, 2018. doi: 10.2514/6.2018-1771.

[79]Chang, R. S. F., Horiguchi, H., and Setser, D. W., "Radiative lifetimes and twobody collisional deactivation rate constants in argon for Kr($4p^55p$) and Kr($4p^55p$) states," *The Journal of Chemical Physics*, Vol. 73, No. 2, 1980, pp. 778–790. doi: 10.1063/1.440185.

[80]O'Haver, T., *A Pragmatic Introduction to Signal Processing*, University of Maryland at College Park, 1997.

[81]Brooks, J., Gupta, A., Smith, M. S., and Marineau, E. C., "Development of Non-Intrusive Velocity Measurement Capabilities at AEDC Tunnel 9," *Proceedings of 52nd Aerospace Sciences Meeting, SciTech*, AIAA-2014-1239, National Harbor, Maryland, 2014. doi: 10.2514/6.2014-1239.

[82]Brooks, J. M., Gupta, A. K., Smith, M. S., and Marineau, E. C., "Development of Particle Image Velocimetry in a Mach 2.7 Wind Tunnel at AEDC White Oak," *Proceedings of 53nd Aerospace Sciences Meeting, SciTech*, AIAA-2015-1915, Kissimmee, Florida, 2015. doi: 10.2514/6.2015-1915.

[83]Brooks, J. M., Gupta, A. K., Smith, M. S., and Marineau, E. C., "PIV Measurements of Mach 2.7 Turbulent Boundary Layer with varying Reynolds Numbers," *Proceedings of 54th Aerospace Sciences Meeting, SciTech*, AIAA-2016-1147, San Diego, California, 2016. doi: 10.2514/6.2016-1147.

[84]Brooks, J. M., Gupta, A. K., Smith, M. S., and Marineau, E. C., "Particle image velocimetry measurements of Mach 3 turbulent boundary layers at low Reynolds numbers," *Experimetns in Fluids - Accepted*.

[85]Bathel, B. F., Danehy, P. M., Inman, J. A., Jones, S. B., Ivey, C. B., and Goyne, C. P., "Velocity Profile Measurements in Hypersonic Flows Using Sequentially Imaged Fluorescence-Based Molecular Tagging," *AIAA Journal*, Vol. 49, No. 9, 2011, pp. 1883–1896. doi: 10.2514/1.J050722.

[86]Hill, R. B. and Klewicki, J. C., "Data reduction methods for flow tagging velocity measurements," *Experiments in Fluids*, Vol. 20, No. 3, 1996, pp. 142–152. doi: 10.1007/BF00190270.

[87]Martin, M. P., "Direct numerical simulation of hypersonic turbulent boundary layers. Part 1. Initialization and comparison with experiments," *Journal of Fluid Mechanics*, Vol. 570, 2007, pp. 347–364. doi: 10.1017/S0022112006003107.

[88]Bradshaw, P., "Compressible Turbulent Shear Layers," *Annual Review of Fluid Mechanics*, Vol. 9, No. 1, 1977, pp. 33–52. doi: 10.1146/annurev.fl.09.010177.000341.

[89]Huang, P. G. and Coleman, G. N., "Van Driest Transformation and Compressible Wall-Bounded Flows," *AIAA Journal*, Vol. 32, No. 10, 1994, pp. 2110–2113. doi: 10.2514/3.12259.

[90]Schlichting, H., *Boundary-Layer Theory*, Springer, 2000.

[91]Morkovin, M. V., "Effects of compressibility on turbulent flows," *Mécanique de la Turbulence*, 1962, pp. 367–380, CNRS.

[92]Klebanoff, P. S., "Characteristics of Turbulence in a Boundary Layer with Zero Pressure Gradient," NACA TR-1247, 1955.

[93]Elena, M., Lacharme, J. P., and Gaviglio, J., "Comparison of hot-wire and laser Doppler anemometry methods in supersonic turbulent boundary layers," *Proceedings of 2nd International Symposium on Laser Anemometry*, Miami Beach, Florida, 1985, pp. 151–157.

[94]Duan, L., Beekman, I., and Martin, M. P., "Direct numerical simulation of hypersonic turbulent boundary layers. Part 3. Effect of Mach number," *Journal of Fluid Mechanics*, Vol. 672, 2011, pp. 245–267. doi: 10.1017/S0022112010005902.

[95]Helm, C., Martin, M. P., and Dupont, P., "Characterization of the shear layer in a Mach 3 shock/turbulent boundary layer interaction," *Journal of Physics: Conference Series*, Vol. 506, No. 1, 2014, pp. 012013. doi: 10.1088/1742-6596/506/1/012013.

[96]Sirovich, L., "Turbulence and the Dynamics of Coherent Structures, Part I: Coherent Structures," *Quarterly of Applied Mathematics*, Vol. 45, No. 3, 1987, pp. 561–571. doi: 10.1090/qam/910462.

[97]Stöhr, M., Sadanandan, R., and Meier, W., "Phase-resolved characterization of vortex–flame interaction in a turbulent swirl flame," *Experiments in Fluids*, Vol. 51, No. 4, 2011, pp. 1153–1167. doi: 10.1007/s00348-011-1134-y.

[98]Knight, B. and Sirovich, L., "Kolmogorov Inertial Range for Inhomogeneous Turbulent Flows," *Physical Review Letters*, Vol. 65, No. 11, 1990, pp. 1356–1359. doi: 10.1103/PhysRevLett.65.1356.

[99]Moser, R. D., "Kolmogorov inertial range spectra for inhomogeneous turbulence," *Physics of Fluids*, Vol. 6, No. 2, 1994, pp. 794–801. doi: 10.1063/1.868317.

[100]Kolmogorov, A. N., "The local structure of turbulence in incompressible viscous fluid for very large Reynolds numbers," Vol. 30, No. 4, 1941, pp. 299–303.

[101]Clemens, N. T. and Narayanaswamy, V., "Low-Frequency Unsteadiness of Shock Wave/Turbulent Boundary Layer Interactions," *Annual Review of Fluid Mechanics*, Vol. 46, 2014, pp. 469–492. doi: 10.1146/annurev-fluid-010313-141346.